

ABSTRACT

MOORE, JOSHUA DANIEL. Single-File and Anomalous Diffusion in Porous Carbons. (Under the direction of Keith E. Gubbins.)

The aim of this project is to obtain a fundamental understanding of single-file and anomalous diffusion in porous carbons. For this purpose we report studies for four different systems: (1) the diffusion of argon in isolated carbon nanotubes; (2) the diffusion of argon/neon, argon/krypton, and argon/xenon mixtures in isolated carbon nanotubes; (3) the diffusion of argon in hexagonally arranged carbon nanotube bundles; and (4) the diffusion of argon in a disordered model of activated carbon and a carbon replica of zeolite. In (1) we find that argon exhibits a mean-squared displacement with a square root of time dependence when the nanotube is small enough in diameter that molecules cannot pass each other. In (2) we find that argon/neon and argon/xenon mixtures exhibit bimodal diffusion in some diameters of carbon nanotubes, where the larger component diffuses in single-file with a square root of time dependence of the mean-squared displacement and the smaller component by a much faster Fickian mechanism with a linear time dependence of the mean-squared displacement. In (1) and (2) the square root of time dependence is observed due to the influence of a stochastic thermostat, which mimics diffusive reflection between the adsorbate atoms and the pore wall. In (3) we observe a square root of time dependence for argon diffusing between carbon nanotubes in the interstitial sites using only microcanonical simulations. Natural corrugation results from the outside walls of the carbon nanotubes. We also show that one-dimensional diffusion within atomically detailed carbon nanotubes can result in artifacts in

the simulation including size correlations and center of mass drift which can only be fully corrected for in the limit of infinite size. When this correction is made, influences including the pore flexibility become negligible for the diffusion of argon. Finally in (4), we observe anomalous, slower modes of diffusion within activated carbon due to argon atoms being trapped within small, highly attractive pores. This is most observable at low relative pressures and short times. In a carbon replica of zeolite, we find that anomalous regions appear at high relative pressures due to argon atoms competing to diffuse through windows and constrictions within the material.

Single-File and Anomalous Diffusion in Porous Carbons

by
Joshua Daniel Moore

A dissertation submitted to the Graduate Faculty of
North Carolina State University
in partial fulfillment of the
requirements for the degree of
Doctor of Philosophy

Chemical Engineering

Raleigh, North Carolina

August 4, 2010

APPROVED BY:

Keith E. Gubbins
Chair of Advisory Committee

Carol K. Hall

Donald W. Brenner

Orlin D. Velev

DEDICATION

To my parents, grandparents, and my brother

BIOGRAPHY

Joshua D. Moore was born on February 14, 1982 in Franklin, Indiana, to his parents Connie Sue Moore and John David Moore. Joshua grew up in Indiana where he attended Indian Creek Senior High School from 1996 until 2000. There he was fortunate to have several excellent teachers including a chemistry and physics teacher named Carol Piety and a calculus instructor named Eugene Kober. Joshua knew that he had a passion for math and science, chemistry especially, and he considered attending college to become a high school math and science teacher, as he spent much of his time tutoring fellow students.

However, when he graduated in 2000, he instead attended Rose-Hulman Institute of Technology in Terre Haute, Indiana majoring in chemical engineering where he was fortunate again to have excellent teachers. These included in chemical engineering, Atanas Serbezov, Sharon Sauer, Ronald Artigue, Daniel Coronell, Hossein Hariri, Mark Anklam, and Alfred Carlson and others including David Erwin, Daniel Jelski, and Howard McLean in chemistry and Diane Evans in mathematics and statistics. Through a chance encounter during a homework assignment in a physical chemistry course, Daniel Jelski recommended Joshua to Atanas Serbezov, with whom he began independent research during his final two years of undergraduate studies modeling adsorption, albeit in a very semi-empirical fashion. Atanas Serbezov has remained a very close mentor to Joshua, especially during his graduate studies. At the same time, Joshua began to immensely enjoy his courses in thermodynamics

with Sharon Sauer. Through encouragement by Alfred Carlson (who said that he would be very disappointed if Joshua did not pursue graduate school) and Howard McClean (who predicted that Joshua would be an academic) as well as guidance from Atanas Serbeozov and Sharon Sauer, Joshua graduated from Rose-Hulman in 2004 with a bachelor's degree in chemical engineering and left Indiana to study chemical engineering at North Carolina State University.

Prior to courses at North Carolina State University, Professor George Roberts gave Joshua employment at North Carolina State University working with Joan Patterson on heat exchanger design and high pressure CO₂ phase equilibria calculations. Beginning classes in the fall of 2004, Joshua had the pleasure of taking courses from Orlin Velez, Saad Khan, Peter Fedkiw, George Roberts, and Keith Gubbins. He also had the opportunity to pursue teaching interests, serving as a teaching assistant for undergraduate honors transport under Gregory Parsons (Fall 2004) and undergraduate (Spring 2005 and 2007) and graduate thermodynamics (Fall 2006 and 2007) courses under Keith Gubbins. In the Fall of 2004, Joshua joined the research group of Professor Keith E. Gubbins, where he carried out the research presented in this thesis. After defending his dissertation, Joshua will become a post-doctoral associate at the Army Research Lab in Aberdeen, Maryland.

ACKNOWLEDGEMENTS

I want to first thank my advisor, Keith E. Gubbins, for offering me his guidance and support at all times. Keith has always given me the support both professionally and personally that I needed to go forward, especially during the many times I wanted to give up. Keith has an amazing insight into science, the academic world, and life in general, and he is always willing to share his experiences with others. I have learned a great deal from him academically and scientifically but more importantly personally through life experiences. He is not only a great academic advisor and mentor but a great friend who I am lucky to know.

I would also like to thank all of the people I have had the privilege to work with, especially my main collaborators, Ying-Chun Liu and Thomas J. Roussel. Without their help and support I would not have been able to complete my Ph.D. Thomas has always been my biggest supporter, and his help both professionally and personally has been very important to me. Without the support of Ying-Chun Liu, I would not have involved myself in this project. It is because of her that I became interested in diffusion, and I have thoroughly enjoyed the work we have done together, along with the work I have done with her student Qu Chen. Much of the work presented here is a result of our collaboration. I am proud of our work together, and I hope that they are as well and have learned from me even a small fraction of what I have learned from them.

I am also grateful to the other members of the Gubbins group both past and present, who have continued to give me the professional and emotional support I needed. These include Jeremy Palmer, who I am ever grateful to and who I have worked with on many interesting problems and hope to continue to work with in the future. I also am grateful to the other current members of the Gubbins group including Liangliang Huang, Yun Long, and Katherine Phillips. Former members of the group include Erik Santiso who I thank for arranging his visit to Raleigh to attend and give me support at my defense. Other former members who I am grateful to include Surendra Jain, Liping Huang, Henry Bock, Milen Kostov, Benoit Coasne, Timothy Morrow, Naresh Chennamsetty, Supriyo Bhattacharya, and others I am sure to have forgotten while I have written this.

I would also like to thank members of the Hall group, especially Johnny Maury, Victoria Wagoner, and Erin Phelps who have always given me more support than they knew. I would like to thank two groups that I have had the privilege to have experiences with. These include Martin Schoen and his group at the Technical University of Berlin in Berlin, Germany, and Qi Wang and his group at Zhejiang University in Hangzhou, China who hosted me during three visits. I would also like to thank my committee for their continued support and patience during the last several years and especially during the final defense. These include Carol Hall, Orlin Velez, Don Brenner, and my advisor Keith Gubbins. I apologize to those I have forgotten, but be sure I am ever grateful to you.

I want to especially thank June McKoy and Sandra Bailey who without I would have never been able to complete anything on time (or almost on time or even late) or know what paperwork to submit. They have always been there to calm me and give me confidence, especially during times when I thought nothing would ever go right.

Finally, I would like to thank Professor George W. Roberts who recently passed. I was never able to tell him the influence he had on me. He convinced me to come to North Carolina State, even though I told him I would not be good enough. He gave me a job when I had nothing else to support myself with before graduate school. He always gave me the support and confidence I needed whenever I saw him, and he never knew that this is what kept me going during many difficult times. I had the privilege of having him for graduate kinetics, and he was absolutely the best teacher I have ever known. I miss him.

The work presented in this thesis was supported by grants from the National Science Foundation (Grant No. CBET-0932656) including an East Asia and Pacific Summer Institute (EAPSI) in China Fellowship (Grant No. 0813060) and computational support through TeraGrid resources provided by the San Diego Supercomputing Center, National Center for Supercomputing Applications, and Indiana University (Grant No. TG-CHE080046N) as well as a U.S. Department of Education Graduate Assistance in Areas of National Need (GAANN) computational fellowship.

TABLE OF CONTENTS

List of Tables	x
List of Figures	xi
Chapter 1. Introduction	1
Chapter 2. Single-file and Fickian Diffusion of Argon in Isolated Single-Walled Carbon Nanotubes	11
2.1. Introduction.....	11
2.2. Model and Simulation Details	12
2.3. Results.....	14
2.4. Conclusion	22
Chapter 3. Bimodal Diffusion of Lennard Jones Mixtures in Isolated Single-Walled Carbon Nanotubes	23
3.1. Introduction.....	23
3.2. Models and Methods.....	24
3.3. Results and Discussion	27
3.3.1. Influence of Pore Diameter and Mixture Composition on Diffusion Mechanism.....	27
3.3.2. Diffusion Coefficients.....	35
3.4. Conclusion	38
Chapter 4. Dual-Mode Diffusion of Argon Confined within Single-Walled Carbon Nanotube Bundles	40
4.1. Introduction.....	40
4.2. Computational Methods.....	43
4.2.1. Grand Canonical Monte Carlo Simulations.....	44
4.2.2. Molecular Dynamics Simulations.....	45
4.3. Results and Discussion	48
4.3.1. Adsorption Isotherm	48
4.3.2. Diffusion Mechanisms.....	49
4.3.3. System Size Effects in Flexible and Rigid Bundles.....	55
4.4. Conclusion	61
Appendix.....	62
Appendix 4A. Correlation Effects and Center of Mass Drifts for Argon Diffusing In Isolated Single-Walled Carbon Nanotubes	63
Chapter 5. Anomalous Diffusion in Ordered and Disordered Microporous Carbons	70
5.1. Introduction.....	70
5.2. Computational Methods.....	73
5.2.1. Monte Carlo Simulations	73
5.2.2. Molecular Dynamics Simulations.....	75
5.3. Results and Discussion	76
5.3.1. Adsorption.....	76

5.3.2. Diffusion	79
5.4. Conclusions.....	84
Chapter 6. Conclusions and Outlook	86
References.....	90

LIST OF TABLES

Table 1.1.	Hopping times between particle passes (τ), diffusivities obtained from transition state theory (D^{tst}) and from MD simulation (D^{sim}) and crossover times predicted from transition state theory (t_c) for the systems shown in Fig. 10. Adapted from ref. ¹⁸	8
Table 3.1.	Densities of Lennard-Jones mixtures (ρ_{mix} , g/cm ³) studied as a function of Ar mole fraction, x_{Ar} , in (6, 6), (7, 7), (8, 8), (9, 9), and (10, 10) single-walled armchair carbon nanotubes at 298 K.	25

LIST OF FIGURES

Figure 1.1.	<p>(a) Mean-squared displacements for single-file LJ fluids ($\sigma_{ff} = 0.383$ nm, $\varepsilon/k = 164$ K, approximately that of CF_4) in perfect cylindrical pores at different system sizes (number of adsorbate particles) for 20 % relative occupancy and 300 K. For small numbers of particles, a finite limiting value of the mean-squared displacement is observed as a result of strong size correlation effects. For larger system sizes, the correlation moves to longer times. These results were from microcanonical MD simulations. The slope of the MSD for the largest system size at long times is 1, which is not the expected result for a single-file fluid (see text). [Adapted from ref. ¹⁰]. (b) Time dependence of the mean-squared displacement for single-file LJ fluids ($\sigma_{ff} = 0.383$ nm, $\varepsilon/k = 164$ K, approximately that of CF_4) in a perfect cylinder at 20 % relative occupancy and 300 K from a microcanonical (N, V, E) MD simulation (line) using 10,000 fluid atoms and a microcanonical MD simulation where random forces have been periodically added to alter the fluid velocities using 4,000 fluid atoms (dashed). The slope of the MSD at the longest times is 1 without random forces but 1/2 when random forces are added. Reference lines (dotted) illustrating t^1 and $t^{1/2}$ dependence of the MSD are also shown. [Adapted from ref. ¹⁰].</p>	4
Figure 1.2.	<p>Mean-squared displacements of LJ particles ($\sigma_{ff} = 0.383$ nm, $\varepsilon/k_B = 164$ K, approximately that of CF_4) in different diameters, d, of perfect cylinders. The fluid-wall interaction was modeled as an inverse Lennard-Jones potential ($u = 4\varepsilon \left[(r/\sigma_T)^{12} - (r/\sigma_T)^6 \right]$, where r is the distance between the axis of the cylinder and the center of a LJ particle and $\sigma_T = (d - \sigma_{ff})/2$) (see ref. ¹⁸). [Adapted from ref. ¹⁸].</p>	8
Figure 1.3.	<p>Self-diffusivity as a function of relative pressure for argon confined at 77K in CS1000A (model of a saccharose based porous carbon) from MD simulation. A maximum in the self-diffusion coefficient exists in the region roughly corresponding to the pore filling region of the isotherm. [Reprinted with permission from ref. ²⁰. Copyright 2006, Taylor & Francis]</p>	10
Figure 2.1.	<p>Adsorption isotherms of argon confined in three types of chiralities in CNTs at 298K. (a) armchair (b) zigzag (c) chiral. In each case the loading is reduced by the accessible volume (Eq. 2.1).</p>	15

Figure 2.2.	Snapshots of GCMC simulations of argon confined in armchair, zigzag and chiral CNTs at 298 K and 30 MPa.	17
Figure 2.3.	(a) Loading of argon in three chiralities of CNTs as a function of the diameter of the CNTs at 298 K at pressures in the range of 0.5MPa to 30 MPa (armchair, open; zigzag, cross; chiral, closed) (b) Loading of argon in three types of CNTs at 298 K as a function of the diameter at 30MPa (armchair, open; zigzag, cross; chiral, closed)....	18
Figure 2.4.	Axial direction mean squared displacement (MSD) of argon confined in (a) armchair (b) zigzag (c) chiral CNTs at 298 K and 30MPa.	20
Figure 2.5.	Transport coefficients of argon as a function of pressure in the various chiralities and diameters of CNTs. (a) single-file mobility, F , and crossover diffusivity, $D_{\text{crossover}}$, (b) Fickian diffusivity.	22
Figure 3.1.	Simulation snapshots in carbon nanotubes consisting of equimolar mixtures of (a) Ar/Ne, (b) Ar/Kr, and (c) Ar/Xe.	28
Figure 3.2.	Axial direction mean squared displacements (MSD) in the indicated CNTs at 298 K in equimolar mixtures for (a) Ar in Ar/Ne mixtures (b) Ne in Ar/Ne mixtures (c) Ar in Ar/Kr mixtures (d) Kr in Ar/Ne mixtures (e) Ar in Ar/Xe mixtures (f) Xe in Ar/Xe mixtures.	30
Figure 3.3.	Axial direction mean squared displacements (MSDs) for Ne, Kr, and Xe in the transition diameter CNTs at 298 K.	33
Figure 3.4.	Axial direction single-file mobilities (a,c,e) and Fickian self-diffusion coefficients (b,d,f) for Ne, Ar, Kr, and Xe in Ar/Ne, Ar/Kr and Ar/Xe mixtures at 298 K in the indicated CNTs.	36
Figure 4.1.	Loading of argon in a (25,0) SWCNT bundle as a function of relative pressure (P/P_o) at 120 K. (a) Adsorption isotherms for all of the atoms in the total bundle (triangles), for only the atoms within the nanotubes (squares) and interstitial adsorbed atoms (circles); (b) snapshots from GCMC simulations at 120 K corresponding to the relative pressures indicated.	50
Figure 4.2.	Mean squared displacement of argon along the axial direction of (25,0) rigid (black) and flexible (red) SWCNT bundles in the nanotubes (dashed), interstitial sites (dashed-dot), and total bundle (line) at 120 K and various relative pressures (P/P_o). System sizes varied by pressure but $\sim 10,000$ interstitial argon atoms were used in each case. In (a) $P/P_o = 1.2 \times 10^{-5}$: there are 10,064 interstitial argon atoms in the simulation and no argon atoms in the nanotubes; in (b) $P/P_o = 6.1 \times 10^{-5}$: there are 10,080 interstitial and 728 nanotube argon atoms; in (c) $P/P_o = 1.2 \times 10^{-4}$: there are 11,820 interstitial and 1,860 nanotube argon atoms; in (d) $P/P_o = 1.2 \times 10^{-2}$: there are 9,360 interstitial and 42,320 nanotube argon atoms.	52

Figure 4.3.	Self-diffusion coefficients for argon diffusing in a rigid and flexible (25,0) SWCNT bundle as a function of relative pressure. The argon atoms in the nanotubes (squares) as well as the total bundle (triangles) exhibit Fickian diffusion and their y-axis is shown on the left. The argon atoms in the interstitial sites (circles) exhibit single-file diffusion and their y-axis is shown on the right. Solid symbols indicate a rigid SWCNT bundle while open symbols indicate a flexible SWCNT bundle. Lines are shown as a guide for the eye.	54
Figure 4.4.	The effect of system size on the mean squared displacement as a function of the total number of argon atoms at $P/P_o = 6.1 \times 10^{-5}$. In (a) and (b) the MSD for argon atoms in the total bundle is compared for the rigid and flexible cases, respectively. In (c) and (d) the MSD for argon atoms in the interstitial sites are compared for the rigid and flexible cases, respectively. The numbers listed on the graphs indicate the total number of argon atoms in the simulation and those in the interstitial sites are in parenthesis. The dashed line illustrates the nominal slope expected for Fickian diffusion in (a) and (b) and single-file diffusion in (c) and (d) with slopes of 1 and 1/2, respectively.	57
Figure 4.5.	The effect of system size on the mean squared displacement as a function of the total number of argon atoms at $P/P_o = 1.2 \times 10^{-2}$. In (a) and (b) the MSD for argon atoms in the total bundle is compared for the rigid and flexible cases, respectively. In (c) and (d) the MSD for argon atoms in the interstitial sites are compared for the rigid and flexible cases, respectively. The numbers listed on the graphs indicate the total number of argon atoms in the simulation and those in the interstitial sites are in parenthesis. The dashed line illustrates the nominal slope expected for Fickian diffusion in (a) and (b) and single-file diffusion in (c) and (d) with slopes of 1 and 1/2, respectively.	58
Figure 4.6.	Mean squared displacement of argon along the axial direction of a (25,0) rigid (black) and flexible (red) CNT bundles in the nanotube channels (dashed), interstitial sites (dashed-dot), and total bundle (line) at 120 K and (a) $P/P_o = 6.1 \times 10^{-5}$ for a system size of 1,158 total argon atoms (1,080 interstitial and 78 nanotube channel atoms) and (b) $P/P_o = 1.2 \times 10^{-2}$ for a system size of 7,752 total argon atoms (1,404 interstitial and 6,348 nanotube channel atoms).	60

Figure 4A.1.	Size correlation and center of mass drift effects for argon diffusing in infinitely long, rigid, (6,6) single-walled carbon nanotubes at 120 K and 3.66×10^{-7} bar. The number in the legend indicates the number of argon atoms diffusing inside the carbon nanotube. Red lines indicate a normal MSD calculation, while black lines indicate a MSD calculation which has had the center of mass subtracted during calculation. Dotted blue lines indicate the nominal slopes expected for single-file (1/2) and Fickian diffusion (1).	64
Figure 4A.2.	The center of mass (COM) drift of argon atoms during microcanonical molecular dynamics simulations for argon in a (6,6) isolated, single-walled carbon nanotube at 120 K and 3.66×10^{-7} bar. System sizes using only 50 or 200 argon atoms show significant center of mass drift, while those with 10,000 and 50,000 argon atoms show smaller drift at longer times.	67
Figure 4A.3.	(a) Argon diffusing in single-file in a (6,6) CNT at 298 K. At 0.01 bar there are 1,536 argon atoms in the microcanonical simulations. At 10 bar, there are 27,904 argon atoms in the microcanonical simulations. (b) Argon diffusing in three-dimensions in a (10,10) CNT at 298 K. At 0.001 bar there are 500 argon atoms in the microcanonical simulations. At 20 bar there are 5,760 argon atoms in the microcanonical simulations. In both figures red lines indicate microcanonical simulations with a flexible CNT wall, black lines indicate microcanonical simulations with a rigid CNT wall. The blue line indicates a canonical simulation using a stochastic Langevin thermostat. In (a) there were 109 argon atoms in the Langevin simulation at 10 bar and in (b) there were 288 argon atoms in the Langevin simulation.	69
Figure 5.1.	Adsorption isotherms for argon at 77 K (closed) and 120 K (open) in C-FAU (circles) and BPL (squares).	77
Figure 5.2.	Pore size distributions for argon in C-FAU and BPL.	78
Figure 5.3.	Simulation snapshots of argon adsorbed in BPL and C-FAU at 120 K and various relative pressures. Snapshots at 77 K are similar for comparable fractional fillings along the isotherm.	79
Figure 5.4.	Mean squared displacements for argon diffusing in BPL activated carbon at various relative pressures, $P/P_o(T)$, at (a) 77 K and (b) 120 K.	80
Figure 5.5.	Mean squared displacements for argon diffusing in C-FAU, the carbon replica of Faujasite, at various relative pressures, $P/P_o(T)$, at (a) 77 K and (b) 120 K.	80
Figure 5.6.	Self-diffusion coefficients for argon in BPL (squares) and C-FAU (circles) at 77 K (open) and 120 K (closed).	84

CHAPTER 1

Introduction

For bulk fluids or fluids which are adsorbed in large pores, diffusion occurs in three dimensionsⁱ. All particles are able to pass each other, their collisions lead to a random walk, and their diffusional mechanism behaves according to Fick's law. When the degree of confinement is enhanced such that the diffusion in three dimensions is restricted, slower modes of diffusion emerge. We refer to these slower modes as *anomalous*, because they do not strictly follow the same behavior as is predicted for diffusion in three dimensions. One way to characterize these slower modes of diffusion is to analyze the time dependence of the mean-squared displacement (MSD). For bulk fluids or fluids which are in pores large enough such that the molecules can pass each other easily in three dimensions, the MSD increases linearly with time. For one dimensional diffusion in a direction z , e.g. along the axis of a carbon nanotube, the MSD can be expressed in terms of the self-diffusion coefficient as:

$$\lim_{t \rightarrow \infty} \left\langle \sum_{i=1}^N [z_i(t) - z_i(0)]^2 \right\rangle = 2D_z t \quad (1.1)$$

ⁱ Some of the material in this chapter has been published in: K.E. Gubbins, Y.C. Liu, J.D. Moore, and J.C. Palmer, "The Role of Molecular Modeling in Confined Systems: Impact and Prospects", To Appear in Physical Chemistry, Chemical Physics, 2010. Reprinted with permission from The Royal Society of Chemistry, Copyright (2010).

In Eq. (1.1) z_i is the position of particle i in a single dimension at time t , D_z is the self-diffusion coefficient of the particles in that dimension, N is the total number of fluid molecules, and the term on the left-hand side in brackets ($\left\langle \sum_{i=1}^N [z_i(t) - z_i(0)]^2 \right\rangle$) is the MSD.

When the fluid becomes confined such that the pore is of a small enough diameter that the motion of the fluid is constrained to a single-dimension and the particles cannot pass each other, a one-dimensional random walk gives rise to a MSD which is predicted¹⁻⁸ to be proportional to the square root of time.

$$\lim_{t \rightarrow \infty} \left\langle \sum_{i=1}^N [z_i(t) - z_i(0)]^2 \right\rangle = 2F_z \sqrt{t} \quad (1.2)$$

In Eq. (1.2), F_z is referred to as the single-file mobility. Experimentally, single-file diffusion has been observed for small molecules in zeolites⁹⁻¹¹, for colloidal particles in confined channels¹²⁻¹⁴ and recently for water in single-walled carbon nanotubes¹⁵.

Theoretically, several groups have been active in the investigation of single-file diffusion. Sholl and Fichthorn¹⁶ have investigated diffusion mechanisms of various fluids in zeolites and found evidence not only of single-file diffusion but also bi-modal diffusion, where one component diffused in single-file and the other by a normal Fickian mechanism. Bi-modal diffusion has also been investigated by Percus and coworkers¹⁷ for hard disks confined

within hard walls. They also extensively investigated single-file diffusion of pure component fluids with hard potentials (hard spheres and hard disks) confined within hard walls¹⁸⁻²⁶.

Hahn and Kärger^{27, 28} investigated single-file diffusion of fluids with continuous potentials in cylindrical pores. They found that there was a significant size correlation effect that occurs for particles diffusing in cylindrical pores. This size effect is shown in Fig. 1.1a. For systems with short file lengths and small numbers of diffusing particles, a finite limiting value of the mean-squared displacement was observed. As the number of diffusing particles was increased with increased length of the pore, this finite value was moved to longer times. Thus, if one is to study single-file diffusion, a large enough system size is needed such that the time at which the finite value of the mean-squared displacement occurs is at a time which is much greater than the needed observation time. From Fig. 1.1a, it is apparent that the number of diffusing particles needed is approximately 10,000 or greater, although the needed system size depends on density²⁹.

Another important observation of Fig. 1.1a, is that the time dependence of the mean-squared displacement is linear for the 10,000 particle system, even though the particles were in single-file confinement. This is due to a violation of a random walk. This is further illustrated in Fig. 1.1b. In Fig. 1.1b, the MSDs for a single-file fluid using a MD simulation in the microcanonical (N, V, E) ensemble with and without random forces added to the adsorbate velocities are shown. The MSD for the microcanonical simulation without random

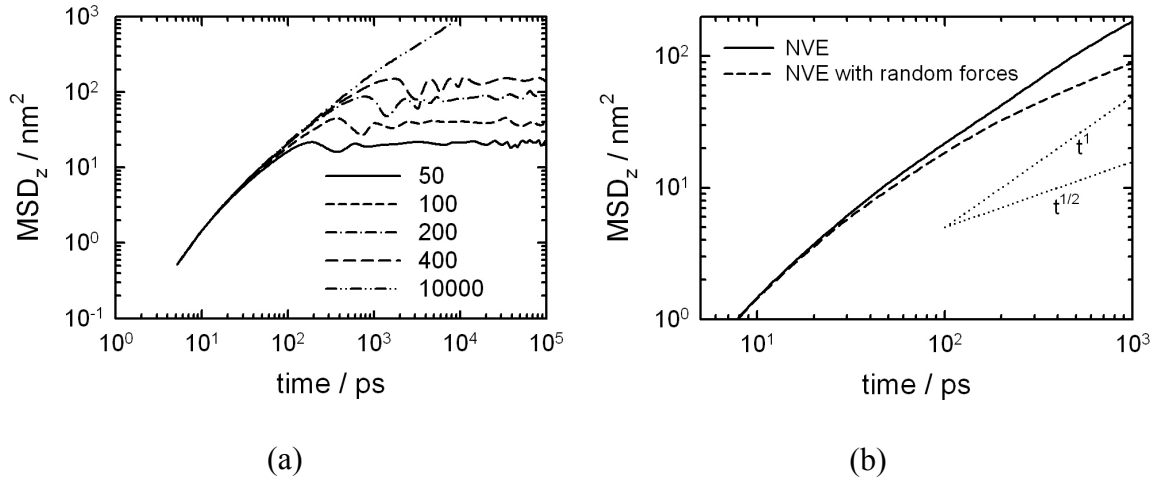


Figure 1.1: (a) Mean-squared displacements for single-file LJ fluids ($\sigma_{ff} = 0.383 \text{ nm}$, $\varepsilon/k = 164 \text{ K}$, approximately that of Kr) in perfect cylindrical pores of effective diameter 0.623 nm at different system sizes (number of adsorbate particles) for 20 % relative occupancy and 300 K . For small numbers of particles, a finite limiting value of the mean-squared displacement is observed as a result of strong size correlation effects. For larger system sizes, the correlation moves to longer times. These results were from microcanonical MD simulations. The slope of the MSD for the largest system size at long times is 1, which is not the expected result for a single-file fluid (see text). [Adapted from ref. ²⁷]. (b) Time dependence of the mean-squared displacement for single-file LJ fluids ($\sigma_{ff} = 0.383 \text{ nm}$, $\varepsilon/k = 164 \text{ K}$, approximately that of Kr) in a perfect cylinder of effective diameter 0.623 nm at 20 % relative occupancy and 300 K from a microcanonical (N, V, E) MD simulation (line) using 10,000 fluid atoms and a microcanonical MD simulation where random forces have been periodically added to alter the fluid velocities using 4,000 fluid atoms (dashed). The slope of the MSD at the longest times is 1 without random forces but 1/2 when random forces are added. Reference lines (dotted) illustrating t^1 and $t^{1/2}$ dependence of the MSD are also shown. [Adapted from ref. ²⁷].

forces exhibits a slope on a log-log scale equal to 1, which would normally be indicative of Fickian diffusion (see Eq. 1.1). However, the fluid is in single-file confinement, and the particles do not pass each other. When a random walk is imposed upon the system by adding

random forces to the particles during the MD simulation, the slope of the MSD on the log-log scale becomes $1/2$, indicative of single-file diffusion (see Eq. 1.2). It can be shown theoretically that the square root of time dependence of the mean-squared displacement results from a random walk², just as it does for Fickian diffusion. Perfectly cylindrical pores, as used in the work of Hahn and Kärger²⁷, are completely smooth. Thus, the standard microcanonical simulations without random forces exhibit purely specular reflection of the particles colliding with the wall, and any diffusive reflection of particles is absent. Because the fluid is constrained in a single dimension, fluid-fluid collisions do not create a random walk. Thus, the absence of a random walk from collisions for fluid-fluid and fluid-wall interactions results in the absence of the square root of time dependence of the MSD. Adding random forces to the particle velocities mimics diffusive collisions, but it is not a real effect for perfectly cylindrical pores.

Another type of system which has been of interest for single-file diffusion are carbon nanotubes²⁹⁻³³. Mao and Sinnott³² found square-root of time dependence of the MSD for fluids diffusing in narrow single-walled carbon nanotubes but used stochastic Langevin thermostats. This thermostat adds random forces to the particles' velocities similarly to the work of Hahn and Karger²⁷, and thus a corrugated pore with diffuse reflections of the particles off the nanotube wall were mimicked. Other researchers who used deterministic thermostats^{31, 33} were not able to observe a square-root of time dependence of the mean-squared displacement for single-file fluids diffusing in carbon nanotubes. These observations

may be related to the fact that carbon nanotubes, similarly to the perfect cylinders previously described, do not result in particles having large amounts of diffusive collisions with the wall. While carbon nanotubes have small amounts of corrugation due to the atomic detail of the wall, this corrugation is not enough to produce diffusive collisions with the walls. Bhatia et al.³⁴ have quantified the diffusive reflection of methane and hydrogen diffusing in atomically detailed carbon nanotubes using a Maxwell coefficient³⁴ which relates specular and diffusive reflections. They found that the fluid-wall collisions were nearly completely specular. The smallest molecule studied, hydrogen, resulted in the greatest amount of diffusive collisions, but these contributed less than 1 % of the total collisions, even at the largest densities studied. Thus, the diffusion of fluids in carbon nanotubes is predicted to be dominated by specular collisions of atoms with the carbon nanotube wall.

Equation (1.2) represents the limiting case of anomalous diffusion which is single-file diffusion. Mao and Sinnott³² have reported dependencies of the mean-squared displacement which are intermediate between the single-file (square root) and Fickian (linear) modes for ethane and ethylene in carbon nanotubes. They found that the smaller, more spherical methane molecule exhibited a completely normal Fickian mode of diffusion, but ethane and ethylene seemed to exhibit a behavior intermediate between single-file and Fickian diffusion. Thus, ethane and ethylene, in some diameters of CNTs, exhibited time dependences of the mean-squared displacement which were between $1/2$ and 1 .

Experimentally, such a transition has not been observed. However, using both simulation and transition state theory, Hahn and Kärger²⁸ presented results that suggested that all diffusion will eventually tend toward the Fickian limit if given enough time. For realistic continuous potentials, the single-file particles will eventually exhibit hopping, as particles begin to hop over their neighbors. The degree of hopping as well as what time scale this occurs on depends entirely on the degree of confinement. Long time (100 ns) MSDs shown in their work are illustrated in Fig. 1.2. Particles in the smallest diameter pores (0.70 and 0.74 nm) exhibited square root of time dependence of their MSDs, indicating single-file diffusion. However, as the pore diameter was increased slightly to 0.78 nm, a transition, similar to that described by Mao and Sinnott³² was observed, where the time dependence of the MSD was between 1/2 and 1. Larger diameter pores exhibited a linear time dependence. Using transition state theory, they estimated particle hopping times in all of the pores. Those in the smallest pores exhibiting single-file diffusion presented hopping on microsecond time scales (beyond the time scale shown in Fig. 1.2 and beyond the current limit of atomistic MD simulations). The particles diffusing in the largest diameter pores exhibited hopping on picosecond time scales which resulted in MSDs with a linear time dependence and nearly complete Fickian diffusion. From transition state theory and hopping times, Hahn and Kärger²⁸ were able to calculate crossover times (the time at which single-file diffusion was predicted to crossover into Fickian diffusion) as well as the predicted diffusion coefficients that would result after this crossover time. These results are shown in Table 1.1. Comparisons are shown between calculated values of the diffusion coefficients from the

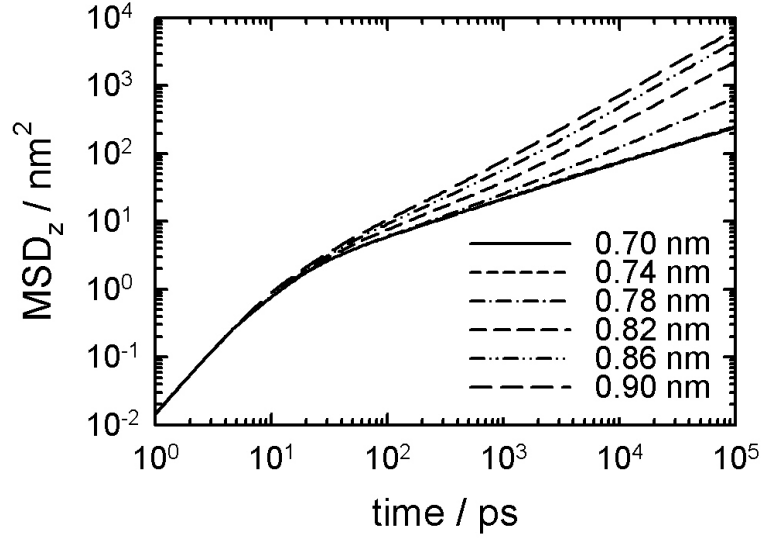


Figure 1.2: Mean-squared displacements of LJ particles ($\sigma_{ff} = 0.383$ nm, $\varepsilon / k_B = 164$ K, approximately that of Kr) in different diameters, d , of perfect cylinders. [Adapted from ref. ²⁸].

Table 1.1: Hopping times between particle passes (τ), diffusivities obtained from transition state theory (D^{tst}) and from MD simulation (D^{sim}) and crossover times predicted from transition state theory (t_c) for the systems shown in Fig. 10. Adapted from ref. ²⁸.

d_T / nm	τ / s	$D^{tst} / \text{m}^2\text{s}^{-1}$	$D^{sim} / \text{m}^2\text{s}^{-1}$	t_c / s
0.70	7.0×10^{-6}	2.6×10^{-13}		3.0
0.74	9.8×10^{-8}	1.9×10^{-11}		5.6×10^{-4}
0.78	5.8×10^{-9}	3.2×10^{-10}		1.6×10^{-6}
0.82	1.5×10^{-10}	1.2×10^{-8}	1.2×10^{-8}	1.3×10^{-9}
0.86	7.1×10^{-11}	2.6×10^{-8}	2.5×10^{-8}	3.0×10^{-10}
0.90	4.5×10^{-11}	4.1×10^{-8}	4.0×10^{-8}	1.2×10^{-10}

MSDs for the largest pores and the calculated values from transition state theory. Excellent agreement was obtained.

Regardless, of whether initial single-file and other anomalous diffusion eventually always result in hopping and Fickian diffusion, the initial slow movement of particles diffusing in pores can influence the overall diffusion coefficients. Anomalous regions in the MSD can result in a maximum in the self-diffusion coefficients for fluids in porous materials, such as activated carbon³⁵. An example is shown in Fig. 1.3 for argon diffusing in a model of a saccharose-derived activated carbon³⁶. In materials with regularly shaped pores, such as carbon nanotubes, the self-diffusion coefficient is expected to decrease with increasing density as an increased density of fluid generally slows diffusion. In disordered porous materials, such as activated carbon, the diffusion of the fluid can be slowed at low densities due to the fluid being adsorbed in strongly attractive pores. As the smallest pores become full at intermediate densities, the larger pores begin to fill and the diffusion rate increases. At higher densities, as the larger pores become filled due to the increased density of the fluid in the pores, the diffusion rate is slowed. This results in a maximum in the self-diffusion coefficient and has been observed in several simulation studies³⁵⁻³⁸ as well as in experiment³⁹.

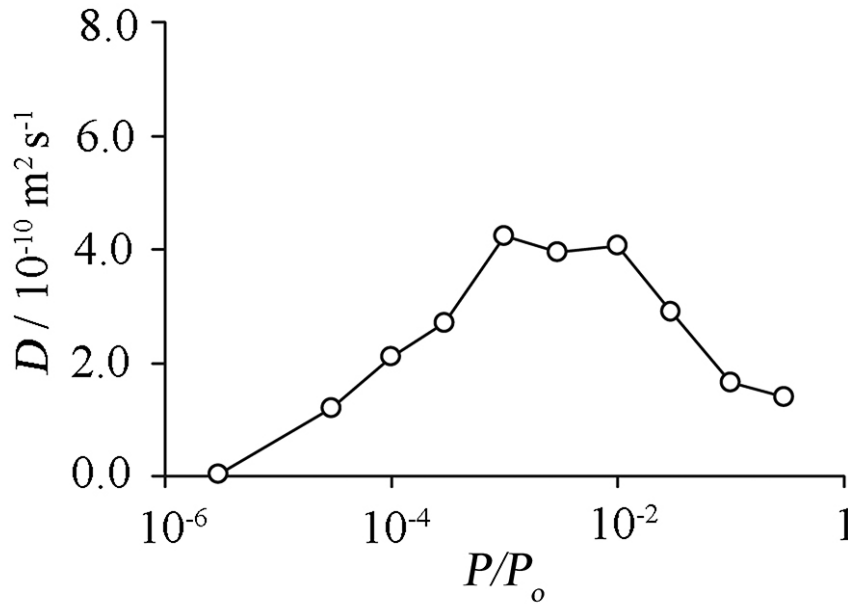


Figure 1.3: Self-diffusivity as a function of relative pressure for argon confined at 77K in CS1000A (model of a saccharose based porous carbon) from MD simulation. A maximum in the self-diffusion coefficient exists in the region roughly corresponding to the pore filling region of the isotherm. [Reprinted with permission from ref. ³⁶. Copyright 2006, Taylor & Francis]

In this thesis, anomalous diffusion is presented in the form of single-file diffusion in carbon nanotubes (Chapters 2 and 3), carbon nanotube bundles (Chapter 4), and in ordered and disordered carbons (Chapter 5) which exhibit anomalous diffusion due to atoms being trapped within small, strongly adsorbing pores or the competition of atoms moving between various constrictions within the material. Finally, in Chapter 6, we present some conclusions regarding the implications of this work and suggest future directions for research in this area.

CHAPTER 2

Single-file and Fickian Diffusion of Argon in Isolated Single-Walled Carbon Nanotubes

2.1 Introductionⁱ

In this chapter we demonstrate that single-file diffusion is possible within narrow single-walled carbon nanotubes. There is a dramatic difference (several orders of magnitude) between the self-diffusion rates of a fluid in Fickian and single-file diffusion. It would be useful to be able to predict when these diffusion mechanisms will occur and the influence that variables such as pore diameter, host flexibility, adsorbate properties, and temperature have on the mechanism. Even though single-file diffusion has been predicted theoretically for decades^{1, 26}, it is still far from well understood. In particular, most investigations involve hard sphere fluids in a model cylindrical pore with hard walls¹⁷⁻²⁵. It is therefore necessary to understand conditions leading to different diffusion mechanisms in realistic models of microporous materials with atomically detailed walls and continuous potentials.

Here we investigate argon diffusing in confined isolated single-walled carbon nanotubes (CNTs) using a combined Grand Canonical Monte Carlo and molecular dynamics study. For

ⁱ Material from this chapter has been published in Y.-C. Liu*, J. D. Moore*, Q. Chen, T. Roussel, Q. Wang and K. E. Gubbins, in *Diffusion Fundamentals III*, eds. C. Chmelik, N. Kanelopoulos, J. Kärger and D. Theodorou, Leipziger Universitätsverlag, Athens, 2009, pp. 164-180.

*Equal Contribution

Ar confined in CNTs, a crossover from single-file to Fickian diffusion is found when the density of Ar is a minimum as a function of the CNT diameter. We show that argon diffuses by a single-file mechanism in CNTs smaller than an accessible diameter of $1.76\sigma_{\text{Ar}}$, corresponding to (7,7), (12,0) and (8,6) CNTs but by a Fickian mechanism for CNTs larger in diameter. In all cases of single-file diffusion the mean-squared displacement (MSD) of the fluid molecules has a square root of time dependence, while molecules diffusing by a Fickian mechanism have a MSD with a linear time dependence.

2.2 Model and Simulation Details

Interactions between the adsorbate molecules as well as between the CNT and the adsorbate molecules were described through a standard (12,6) Lennard-Jones potential. The CNTs are rigid with the carbon atoms held fixed and are given zero velocity in the MD simulations. Parameters for argon were taken from Skoulidas and Sholl⁴⁰ ($\sigma_{\text{Ar}} = 0.342$ nm, $\epsilon_{\text{Ar}} / k_{\text{b}} = 124.07$ K) and for carbon from Steele⁴¹ ($\sigma_{\text{C}} = 0.34$ nm, $\epsilon_{\text{C}} / k_{\text{b}} = 28.0$ K). All cross interactions were obtained through the usual Lorentz-Berthelot combination rules.

Grand Canonical Monte Carlo simulations (GCMC) were performed to compute argon adsorption isotherms in CNTs at 298 K. The fluid was restricted to adsorbing in the inner channels of the CNTs only. Several chiralities (armchair, zigzag and chiral) of CNTs, based on the two indices (n,m) of the Hamada classification⁴², were studied. The armchair (m,m) CNTs had indices of $n = 6, 7, 8, 9, 10$, corresponding to diameters of 0.81, 0.95, 1.08, 1.22,

and 1.35 nm, respectively. The zigzag $(n, 0)$ CNTs had indices of $n = 10, 11, 12, 13, 14, 15$, corresponding to diameters of 0.78, 0.86, 0.94, 1.02, 1.09, 1.17 nm, respectively. The chiral (m, n) CNTs had chiral indices of $m = 7, 8, 9, 10, 11$ and $n = 5, 6, 7, 8, 9$, corresponding to diameters of 0.82, 0.95, 1.09, 1.22, and 1.36 nm, respectively. In the GCMC simulations, the nanotube lengths were 9.83 nm, 11.08 nm, and 8.90 to 14.76 nm in length for the armchair (m, m) , zigzag $(n, 0)$, and chiral (n, m) geometries, respectively. The isotherm was measured in the range 8×10^{-5} to 30 MPa, the latter being a pressure at which all of the tubes were completely filled with adsorbate.

The molecular dynamics (MD) simulations for this set of simulations were performed using the NAMD (NAnoscale Molecular Dynamics) simulation package⁴³ using a stochastic Langevin thermostat with a damping coefficient of 1 ps^{-1} . The implications of using a stochastic thermostat have been discussed^{29, 44}, and one is used for two reasons. The first is that it mimics fluid-wall momentum exchange through the inclusion of random damping of the fluid velocities. The second reason is that it provides an effective corrugated surface so that diffuse reflections of the atoms are mimicked, so that the slower square-root of time dependence of the mean-squared displacement (MSD) is observed for single-file diffusion. Without this effective corrugation, the collisions of Lennard-Jones atoms off the wall of pristine carbon nanotubes would all be nearly specular³⁴, and the random walk required to observe the square-root of time dependence of the MSD in single-file diffusion would be violated²⁷.

Another benefit to using the Langevin thermostat is that significantly smaller system sizes than are required in microcanonical simulations could be used²⁹. This was especially true for the single-file systems which have long range spatial correlations²⁷ (see Chapter 4). When no thermostat was used, microcanonical (N,V,E) simulations were found to need 10,000 fluid atoms or more²⁹, especially for single-file fluids which have dramatic long range correlations of the velocities.

The configurations from the GCMC simulations were used as a starting configuration for the MD simulations, but were replicated five times in the axial (z) direction of the nanotube. This corresponded to a range of 114 to 840 fluid atoms in the simulations. The MD simulations were performed using an equilibration period of at least 2 ns followed by a production run of at least 10 ns using a 1 fs timestep. The mean-squared displacement was measured in the axial direction of the nanotube from the trajectory of the production run. Periodic boundary conditions were used in the axial direction of the nanotube.

2.3 Results

The adsorption isotherms of argon confined in three types of chiralities of CNTs at 298 K were calculated from GCMC simulations and are shown in Fig. 2.1. The loading is normalized using the accessible volume from:

$$V_i^{acc} = \frac{\pi}{4} L \left[d_t - \left(\frac{\sigma_c + \sigma_i}{2} \right) \right]^2 \quad (2.1)$$

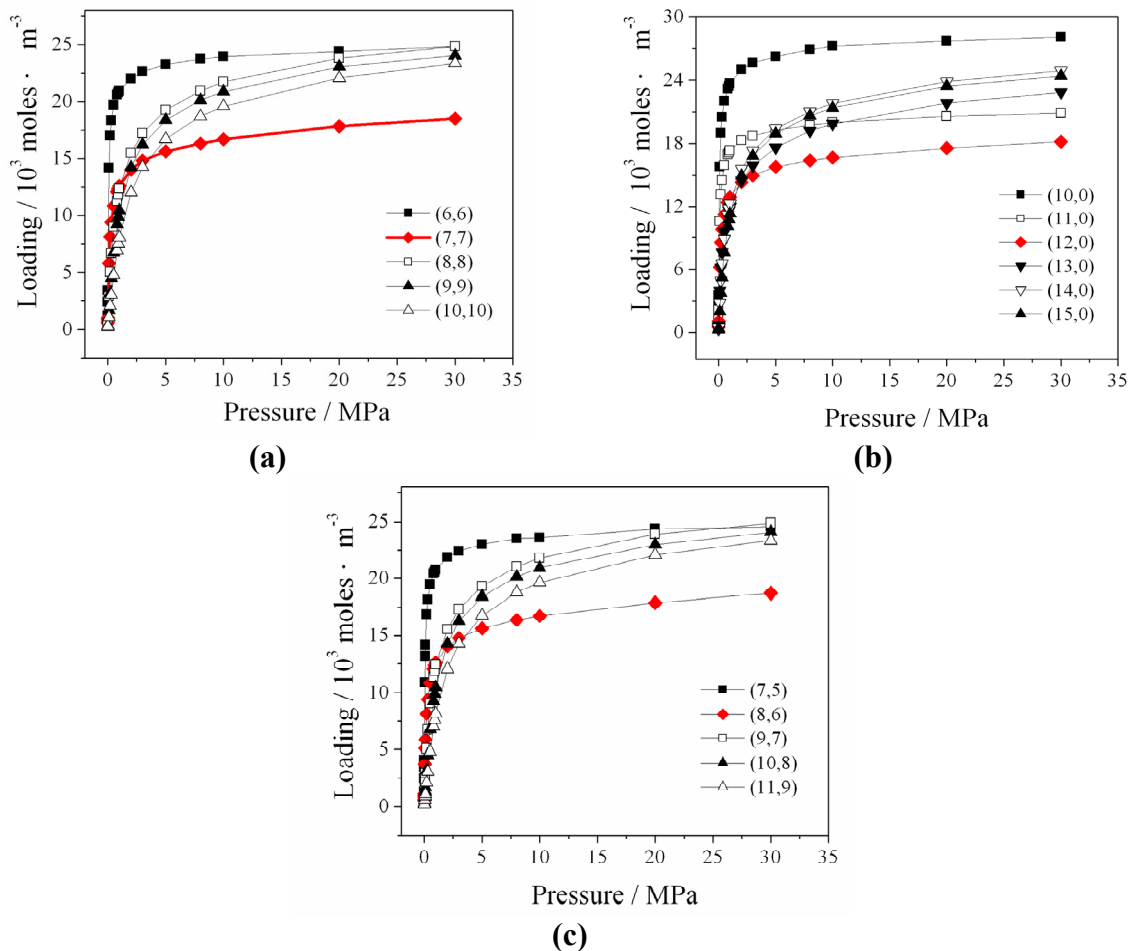


Figure 2.1: Adsorption isotherms of argon confined in three types of chiralities in CNTs at 298K. (a) armchair (b) zigzag (c) chiral. In each case the loading is reduced by the accessible volume (Eq. 2.1).

We observe a general trend that the loading decreases with increasing tube diameter, as it is less confined. However, in the (7,7), (12,0) and (8,6) tubes, the loading is at a minimum compared to the other tubes. In these tubes, the diameter has increased compared to the (6,6), (10,0) and (7,5) CNTs, but there is not enough space for a second molecular layer of fluid to adsorb. Therefore, the ratio of the amount of fluid adsorbed with respect to the

accessible volume has decreased. In the zigzag chirality, there are two minimum diameters, (11,0) and (12,0) as this chirality of CNT has a smaller increase in diameter compared to the other chiralities studied (armchair or chiral).

Several example configurations are shown as simulation snapshots in Fig. 2.2 at 30 MPa and 298 K. In the (6,6), (10,0) and (7,5) CNTs (diameters of approximately 0.8 nm), only a single molecular layer of fluid is adsorbed and this layer is almost linear along the CNT axis. As the diameter increases slightly in the (7,7), (12,0) and (8,6) CNTs (diameters of approximately 0.94 nm, accessible diameter approximately $1.76\sigma_{Ar}$), the fluid no longer aligns linearly with respect to the axial direction of the tube. However, the accessible volume is not large enough for a second molecular layer of fluid to form. As the diameter is increased further in the (9,9), (15,0) and (10,8) CNTs with geometric diameters of approximately 1.2 nm, two molecular layers of fluid have formed.

Because the (7,7), (12,0) and (8,6) CNTs have the largest diameters that exhibit the single molecular layer of fluid, we refer to these as the “transition” or “crossover” CNTs. All CNTs studied with diameters larger than these transition nanotubes exhibited at least two molecular layers of fluid. We also find that the adsorption energy profiles of argon in (6,6), (10,0) and (7,5) exhibit one energy minima while the energy profiles in the (7,7), (12,0) and (8,6) CNTs exhibit two energy minimum. The adsorption energy profiles of argon in CNTs larger than the transition CNT diameter exhibit at least two energy minima.

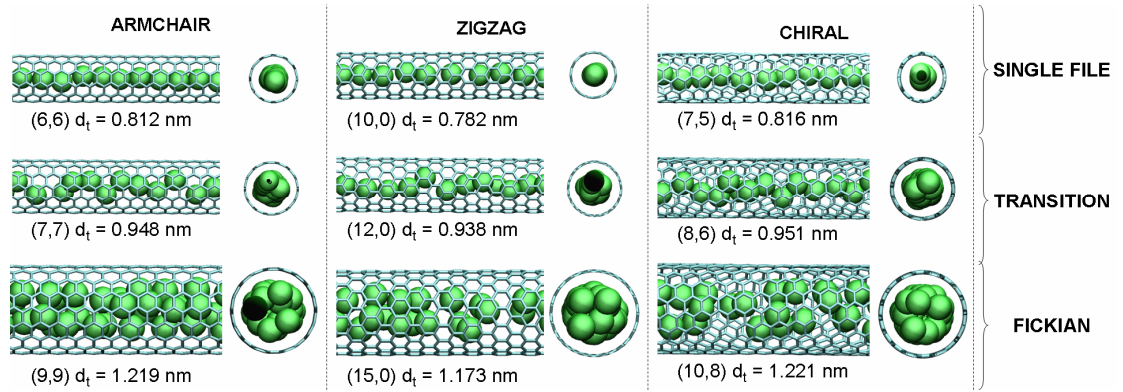


Figure 2.2: Snapshots of GCMC simulations of argon confined in armchair, zigzag and chiral CNTs at 298 K and 30 MPa.

A second analysis of the isotherm can be obtained by plotting the accessible loading as a function of the CNT diameter. This is shown in Fig 2.3 (a). A minimum in the loading occurs at a diameter of approximately 0.94 nm. This is the diameter corresponding to the (7,7), (12,0) and (8,6) CNTs (the transition CNTs). In Fig 2.3(b) we show the same plot, but only at 30 MPa for clarity. We find that below approximately 2 MPa, this minima in the loading disappears. Therefore, we have limited our MD study to pressures above 2 MPa. Mon and Percus found a minimum in the density for hard sphere fluids in perfect cylinders with hard walls. They obtained a minimum in the density at a diameter of approximately $2.16\sigma_{HS}$. Our result is similar despite the fact that we are using a Lennard-Jones potential for the fluid-wall interaction. We found that the minima is at $2.76\sigma_{Ar}$ based on the geometric diameter of the CNT or $1.76\sigma_{Ar}$ when the accessible diameter is taken into account from Eq. (2.1). We can conclude that the ratio of the diameter of the fluid molecule compared to the

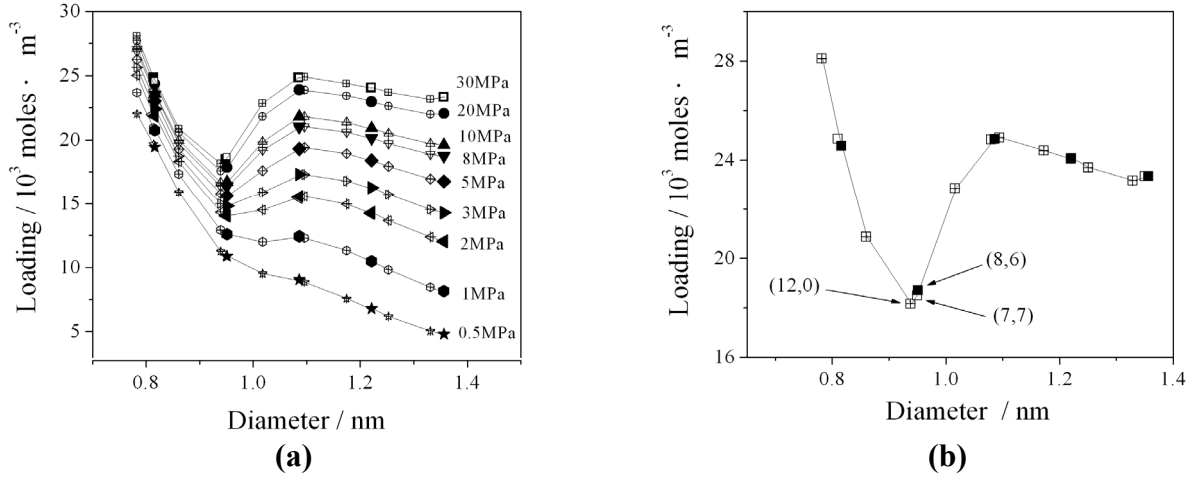


Figure 2.3: (a) Loading of argon in three chiralities of CNTs as a function of the diameter of the CNTs at 298 K at pressures in the range of 0.5MPa to 30 MPa (armchair, open; zigzag, cross; chiral, closed) (b) Loading of argon in three types of CNTs at 298 K as a function of the diameter at 30MPa (armchair, open; zigzag, cross; chiral, closed)

CNT diameter is an important factor in determining whether the fluid adsorbs in a single molecular layer.

Diffusive motions in pores can occur by several fundamentally different mechanisms, including ballistic motion (Eq. 2.2), Fickian diffusion (Eq. 2.3), and single-file diffusion (Eq. 2.4).

$$\lim_{t \rightarrow 0} \left\langle [z(t) - z(0)]^2 \right\rangle = 2E_z t^2 \quad (2.2)$$

$$\lim_{t \rightarrow \infty} \left\langle [z(t) - z(0)]^2 \right\rangle = 2D_z t \quad (2.3)$$

$$\lim_{t \rightarrow \infty} \langle [z(t) - z(0)]^2 \rangle = 2F_z \sqrt{t} \quad (2.4)$$

In Eqns. 2.2-2.4, z is the distance along the axial direction of the pore, the left hand side of these equations is the mean squared displacement of a molecule in time t , E_z is the ballistic mobility constant, F_z is the single-file mobility, and D_z is the familiar Fickian self-diffusion coefficient.

Clearly ballistic motion is much faster than Fickian diffusion, which is in turn much faster than single-file diffusion; the latter occurs when the pore is too narrow to allow molecules to pass each other. All three mechanisms are seen in our MD simulations. It is important to know which diffusion mechanism is occurring in the material. Many materials of current interest have a bi- or tri-modal pore distribution, so that more than one mechanism may be occurring in different regions of the material at the same time

Figure 2.4 shows the MSD of argon as a function of time in three chiralities of CNTs at 30MPa. For all tubes, if the time is shorter than 1 ps, the MSD exhibits approximately ballistic motion. As time increases, in the larger tubes, which have diameters larger than 1.1 nm, the motion is Fickian, with the MSD proportional to time. For the small tubes with diameters of 0.814, 0.783 and 0.816 nm corresponding to the (6,6), (10,0) and (7,5) CNTs, respectively, the MSDs are proportional to the square root of time, typical of single-file diffusion (SFD). The intermediate tubes with diameters of 0.949, 0.939 and 0.951 nm

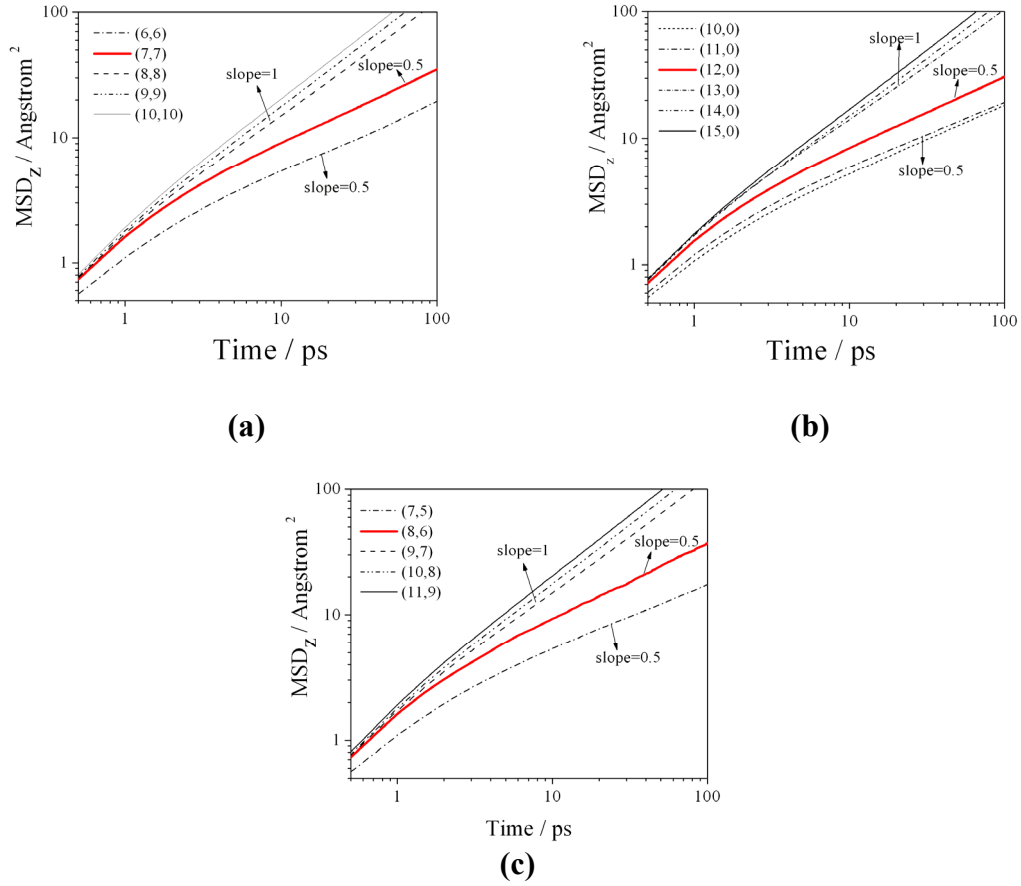


Figure 2.4: Axial direction mean squared displacement (MSD) of argon confined in (a) armchair (b) zigzag (c) chiral CNTs at 298 K and 30MPa.

corresponding to the transition CNTs of (7,7), (12,0) and (8,6), respectively, also have MSDs proportional to the square root of time. However, even though the MSD still is proportional to the square root of time in the transition CNTs, which indicates SFD, the MSD is much larger compared to the (6,6), (10,0) or (7,5) CNTs. The location of the MSDs of the transition CNTs is intermediate between the Fickian and the smallest SFD CNTs, and a crossover from single-file to Fickian diffusion occurs.

Note that in Fig. 2.4, we have only shown the MSDs to 100 ps. As we have used a Langevin thermostat, which makes use of modifying the velocities randomly to correct the temperature, we have overcome some of the aspects associated with the finite size effects previously shown by Hahn and Karger²⁷ in single-file diffusion. Because of this, we were able to observe the $t^{1/2}$ dependence for the single-file fluids in the range of 10 to 100 ps for systems of the order of 100 atoms. However, the system size effects still exist and present themselves for times on the order of 1 ns for this system size.

In Fig. 2.5, three types of transport coefficients are shown as a function of pressure for different CNTs. All coefficients decrease as pressure increases and increase as tube size increases in the same chirality of CNT. We compared the coefficients for the crossover and the single-file mobility for SFD which have the same units and magnitude. The diffusivities for the crossover point are larger than the SFD mobilities. The Fickian diffusivity is greater by four orders of magnitude than the single-file mobility, E , and crossover diffusivity. At these conditions, the effect of the chirality of the CNTs is negligible. This is because the fluid-wall energy differences are small compared to kT for argon in these different chiralities at 298 K. For other fluids, such as water, the difference between diffusion coefficients in different chiralities of CNTs at 298 K have been shown to be quite pronounced⁴⁵.

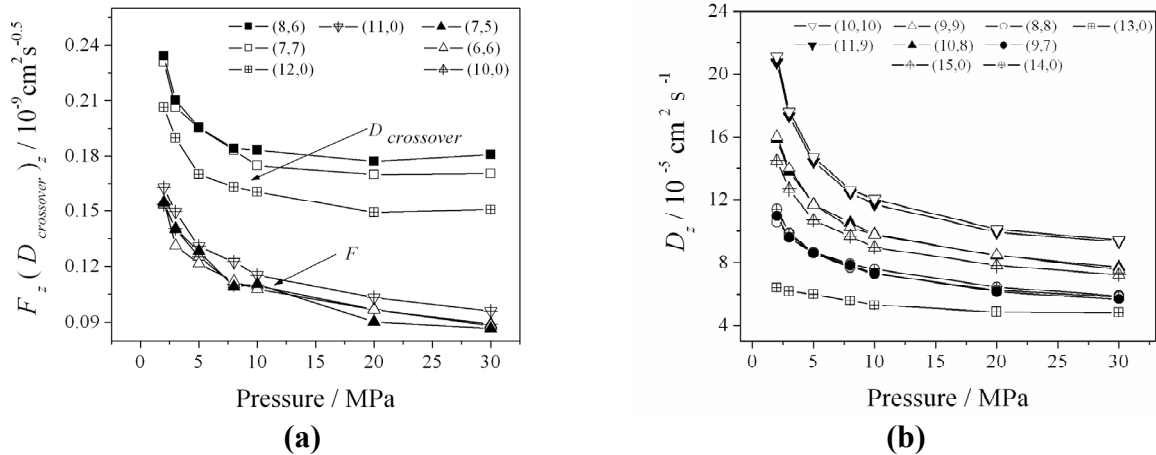


Figure 2.5: Transport coefficients of argon as a function of pressure in the various chiralities and diameters of CNTs. (a) single-file mobility, F , and crossover diffusivity, $D_{\text{crossover}}$, (b) Fickian diffusivity.

2.4 Conclusion

Carbon nanotube structures provide a model to investigate the diffusion mechanism of self-diffusion known to occur in small pores. Ballistic motion always occurs for short times (sub-picosecond), and Fickian or single-file diffusion occurs at longer times depending on the pore size. We found that argon diffuses in single-file for CNT diameters less than approximately 0.94 nm or approximately $1.76\sigma_{\text{Ar}}$ in accessible diameter, corresponding to (7,7), (12,0) and (8,6) CNTs in our study. For CNTs with diameters larger than these, we observe Fickian diffusion. Previous studies have reported slopes of the MSD on the log-log scale between 1/2 and 1 for chain molecules diffusing in CNTs³², but despite analyzing incrementally increasing pore diameters, we found that the slope does not deviate from 1/2 for single-file diffusion and 1 for Fickian diffusion for argon.

CHAPTER 3

Bimodal Diffusion of Lennard Jones Mixtures in Isolated Single-Walled Carbon Nanotubes

3.1 Introductionⁱ

In Chapter 2, we demonstrated that single-file diffusion was possible within narrow single-walled carbon nanotubes (CNTs) using a stochastic Langevin thermostat. This study is continued in this chapter with the investigation of binary mixtures of Lennard-Jones fluids (Ar/Ne, Ar/Kr, and Ar/Xe) diffusing in armchair carbon nanotubes. Our main focus is to determine the carbon nanotube diameter at which various fluids cross-over from single-file to Fickian diffusion and what diameter of the nanotube is predicted to give rise to bimodal diffusion, where one component diffuses by a single-file mechanism and the other by a Fickian mechanism. A range of effects are examined including the mixture concentration, the size ratio of the two components, and the nanotube diameter.

Recently, Ball *et al.* have demonstrated bimodal diffusion for hard disks diffusing in structureless cylindrical pores¹⁷ in which one type of disk diffused by a single-file mechanism

ⁱ Material from this chapter has been published in Q. Chen*, J.D. Moore*, Y.C. Liu, T.J. Roussel, Q. Wang, W. Tao, and K.E. Gubbins, "Transition from Single-File to Fickian Diffusion for Binary Mixtures in Single-Walled Carbon Nanotubes", In Press, Journal of Chemical Physics, 2010. Reprinted with permission from the American Institute of Physics, Copyright (2010).

*Equal Contribution

and the other by a Fickian mechanism. Other simulation studies of binary mixtures of small molecules diffusing through AlPO₄-5 zeolites gave rise to bimodal diffusion for some mixtures¹⁶. However, to our knowledge a systematic study of bimodal diffusion in atomically detailed carbon nanotubes with realistic continuous potentials has not been performed. Nevertheless, the implication of the diffusion mechanisms where bimodal diffusion occurs is still scarcely understood and could be useful in a variety of applications.

3.2 Models and Methods

A series of rigid armchair (n, n) single-walled carbon nanotubes were chosen with indices of $n = 6, 7, 8, 9, 10$, equivalent to geometric tube diameters, d_T (defined as the distance between the centers of surface carbon atoms on opposing walls), of 0.812, 0.948, 1.08, 1.22 and 1.35 nm, respectively. The nanotubes were solvated with binary mixtures of Lennard-Jones (LJ) fluids (Ar/Ne, Ar/Kr and Ar/Xe). The mole fraction of each mixture was varied in each tube from $x_{Ar} = 0$ to 1. The mass density of the mixture (Ar/B where B is the second component in the mixture) was defined as:

$$\rho_{mix} = \frac{1}{N_{Av}} \left(\frac{N_{Ar} MW_{Ar} + N_B MW_B}{x_{Ar} V_{Ar}^{acc} + x_B V_B^{acc}} \right) \quad (3.1)$$

where V_i^{acc} is the pore volume accessible to molecules of component i , given by:

$$V_i^{acc} = \frac{\pi}{4} L \left[d_T - \left(\frac{\sigma_C + \sigma_i}{2} \right) \right]^2 \quad (3.2)$$

In Eqns. (3.1) and (3.2) N_i and MW_i are the number of molecules and molecular mass of component i , respectively, L is the length of the nanotube, and d_T its diameter.

The accessible volume is an estimate based upon the diameter of the nanotube, the length of the nanotube, and an estimate of the excluded volume at the wall. The estimate in Eqn. (3.2) is based on the Lorentz combining rule for the cross interaction, σ_{ij} .

$$\sigma_{ij} = \frac{\sigma_i + \sigma_j}{2} \quad (3.3)$$

The densities of the mixtures used are shown in Table 3.1 for mixtures of Ar/Kr, Ar/Ne and Ar/Xe. Lennard-Jones parameters were used for carbon ($\sigma_C = 0.340$ nm, $\varepsilon_C/k_b = 28.0$ K)⁴¹, for Ar ($\sigma_{Ar} = 0.342$ nm, $\varepsilon_{Ar}/k_b = 124.1$ K)⁴⁶, for Ne ($\sigma_{Ne} = 0.279$ nm, $\varepsilon_{Ne}/k_b = 35.7$ K)⁴⁰, for Kr ($\sigma_{Kr} = 0.361$ nm, $\varepsilon_{Kr}/k_b = 161.0$ K)⁴⁶, and for Xe ($\sigma_{Xe} = 0.410$ nm, $\varepsilon_{Xe}/k_b = 221.0$ K)⁴⁰. All cross interactions were obtained with the Lorentz-Berthelot combining rules.

Table 3.1: Densities of Lennard-Jones mixtures (ρ_{mix} , g/cm³) studied as a function of Ar mole fraction, x_{Ar} , in (6, 6), (7, 7), (8, 8), (9, 9), and (10, 10) single-walled armchair carbon nanotubes at 298 K.

	x_{Ar}						
	0	0.1	0.3	0.5	0.7	0.9	1
Ar/Ne	0.21	0.24	0.30	0.35	0.41	0.46	0.49
Ar/Kr	1.26	1.18	1.03	0.87	0.72	0.56	0.49
Ar/Xe	2.27	2.09	1.73	1.38	1.02	0.67	0.49

Three mixtures were employed in this investigation. Relative to Ar, one mixture contained a second component which was smaller in size (Ne), another only slightly larger (Kr), and another which was substantially larger in size (Xe). Simple Lennard-Jones fluid mixtures were chosen so that trends of the carbon nanotube transition diameters might be more easily interpreted.

Molecular dynamics (MD) simulations were performed using the NAMD (NANoscale Molecular Dynamics) package⁴³. A time step of 2 fs was used with atom coordinates saved every 1 ps during the simulation. A cutoff of 12 Å was used for the potentials with a smoothing function utilized from 10 Å to 12 Å, allowing for both the energy and the force of the LJ potential to smoothly go to zero without any discontinuities. The temperature was maintained at 298 K using a stochastic Langevin thermostat with a damping coefficient of 1 ps⁻¹.

As in chapter 2, a stochastic Langevin thermostat is used for the reason that it provides an effective corrugated surface by mimicking fluid-wall momentum exchange through the inclusion of random damping. This allows for the square-root of time dependence of the MSD to emerge through mimicked diffuse reflections with the carbon nanotube wall. It also allows significantly smaller system sizes to be used than are required in microcanonical simulations²⁹. This was especially true for the single-file systems which have long range spatial correlations²⁷.

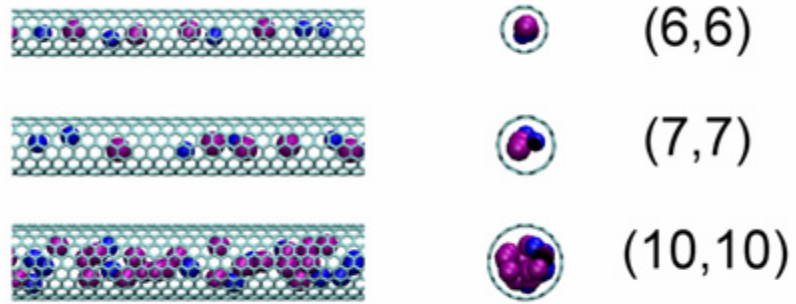
Each nanotube was modeled as infinitely long with periodic boundary conditions in the axial direction. In order to increase the number of particles and reduce system size effects²⁷,²⁹, the nanotubes were 2.46 nm in length. This produced configurations ranging from 315 to 1,925 fluid atoms in the simulations. The MD simulations were performed using an equilibration period of at least 2 ns, followed by a production run of at least 10 ns. The MSD was measured in the axial direction of the nanotube with multiple time origins from the trajectory of the production run.

3.3 Results and Discussion

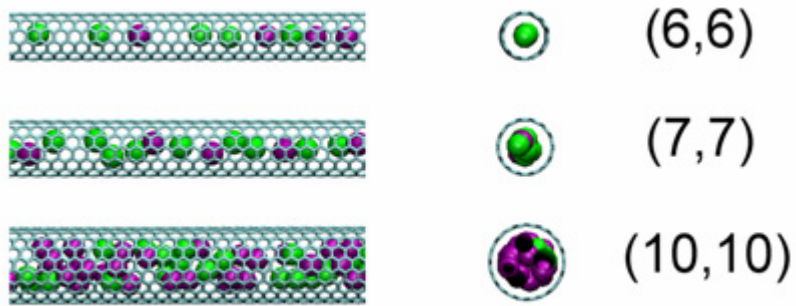
3.3.1 Influence of Pore Diameter and Mixture Composition on Diffusion Mechanism

Simulation snapshots are shown in Fig. 3.1 for 50 mole % argon mixtures in various diameters of carbon nanotubes. In the smallest carbon nanotubes, for each mixture, a single, almost linear molecular layer of fluid was formed in each carbon nanotube. As the diameter of the nanotube increased, a second layer of fluid eventually formed.

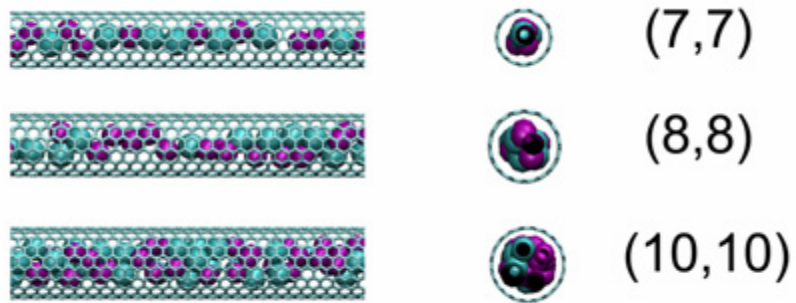
For each component in the mixtures (*i.e.*, Ar/Ne, Ar/Kr, or Ar/Xe) we have calculated the mean-squared displacement (MSD). These are shown in Fig. 3.2 for equimolar mixtures in each tube. We note that the MSDs are only shown up to a time scale of 100 ps. Since a stochastic Langevin thermostat was employed, which controlled the temperature through



(a) Argon (purple) / Neon (blue)



(b) Argon (purple) / Krypton (green)

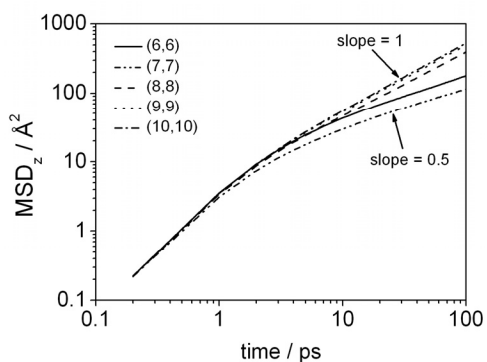


(c) Argon (purple) / Xenon (cyan)

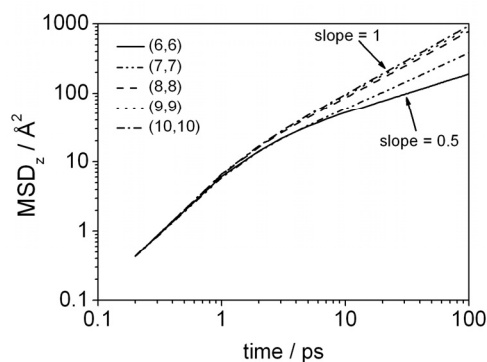
Figure 3.1: Simulation snapshots in carbon nanotubes consisting of equimolar mixtures of (a) Ar/Ne, (b) Ar/Kr, and (c) Ar/Xe.

random modification of the velocities, some of the aspects associated with finite size effects^{27, 29} in single-file diffusion were improved. Thus, we were able to observe the square-root of time dependence of the MSD for single-file fluids in the range of ~ 10 to 100 ps for system sizes on the order of 100 atoms. However, system size effects still existed and presented themselves for times greater than ~ 100 ps.

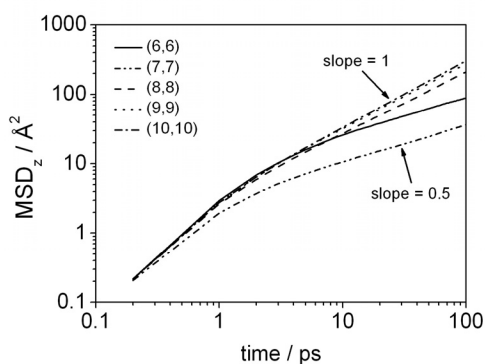
For all of the MSDs shown in Fig. 3.2, the MSD was proportional to the square of time at sub-picosecond times, indicating ballistic motion (free-flight). As the time increased, the MSD either approached a linear time dependence (indicating Fickian diffusion) or a square root of time dependence (indicating single-file diffusion (SFD)). In the Ar/Ne mixture (Figs. 3.2(a) and 3.2(b)), Ar was observed to have a MSD proportional to the square root of time in the (6, 6) and (7, 7) CNTs, indicative of SFD, and a MSD proportional to time in the (8, 8), (9, 9), and (10, 10) CNTs, indicative of Fickian diffusion. Neon also was observed to obey a square root of time dependence of the MSD in the (6, 6) CNT, indicative of SFD, and a MSD proportional to time in the (7,7), (8,8), (9,9) and (10,10) CNTs, indicative of Fickian diffusion. Therefore, in the case of the (7,7) CNT, the Ar/Ne mixture provided an example of bimodal diffusion, where the larger fluid component (Ar, $\sigma_{\text{Ar}} = 0.342$ nm) exhibited single-file diffusion while the smaller component (Ne, $\sigma_{\text{Ne}} = 0.279$ nm) exhibited Fickian diffusion.



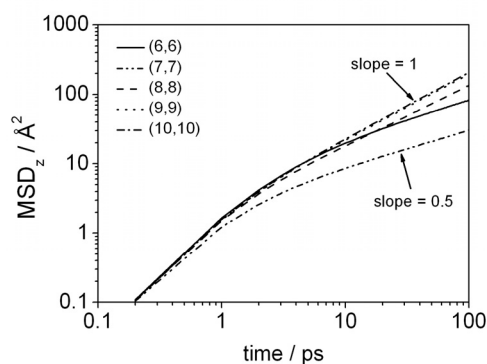
(a) Ar in 50% Ar/Ne mixture



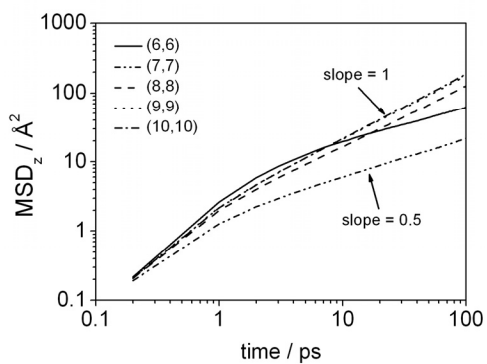
(b) Ne in 50% Ar/Ne mixture



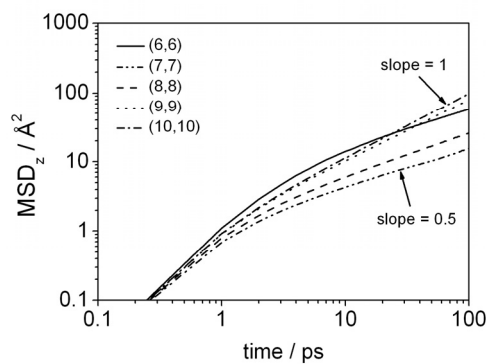
(c) Ar in 50% Ar/Kr mixture



(d) Kr in 50% Ar/Kr mixture



(e) Ar in 50% Ar/Xe mixture



(f) Xe in 50% Ar/Xe mixture

Figure 3.2: Axial direction mean squared displacements (MSD) in the indicated CNTs at 298 K in equimolar mixtures for (a) Ar in Ar/Ne mixtures (b) Ne in Ar/Ne mixtures (c) Ar in Ar/Kr mixtures (d) Kr in Ar/Ne mixtures (e) Ar in Ar/Xe mixtures (f) Xe in Ar/Xe mixtures.

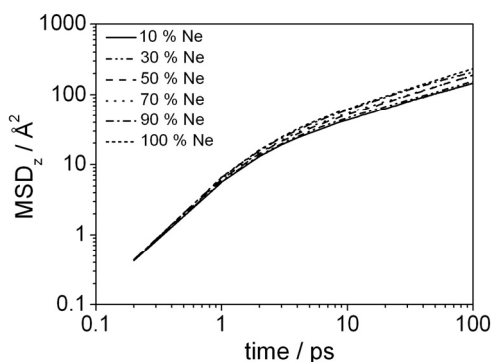
In the Ar/Kr mixture (Figs. 3.2(c) and 3.2(d)), both Ar and Kr were similar in size ($\sigma_{\text{Ar}} = 0.342$ nm, $\sigma_{\text{Kr}} = 0.361$). In the (6,6) and (7,7) CNTs, both components exhibited single-file diffusion as shown in Fig. 3.2(c) for Ar and Fig. 3.2(d) for Kr. In larger diameter CNTs ((8,8), (9,9), and (10,10)), the diffusion mechanism of both Ar and Kr can be characterized as being Fickian, as both molecules can freely pass each other in 3-dimensions.

In the Ar/Xe mixture (Figs. 3.2(e) and 3.2(f)), Xe was larger than Ar ($\sigma_{\text{Ar}} = 0.342$ nm, $\sigma_{\text{Xe}} = 0.410$ nm). Argon diffused by the same mechanism as in the other mixtures. However, Xe diffused by a single-file mechanism in the (6,6), (7,7) and (8,8) CNTs and by a Fickian mechanism in the (9, 9) and (10, 10) CNTs. Therefore, we observed a bimodal diffusion mechanism in the (8, 8) CNT since Ar diffused by a Fickian mechanism while Xe diffused by a single-file mechanism.

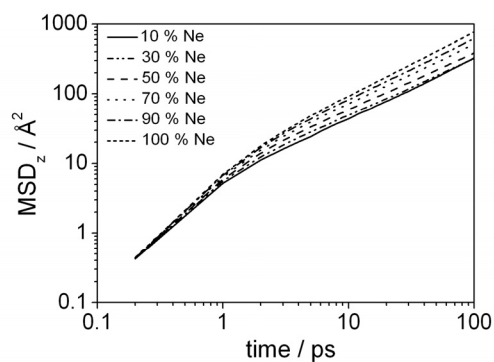
The MSD for Ar in the (6, 6) CNT was greater than that in the (7, 7) CNT and was smaller than that in (8, 8) CNT (Fig. 3.2a). A similar observation was made for Xe diffusing in the (8, 8) CNT, which had a MSD greater than the (7,7) CNT but less than the MSD in the (6,6) CNT. It might be expected that the diffusional rate (and thus the MSD) should increase with increasing CNT diameter. This was the observed result for atoms diffusing by a Fickian mechanism in the larger diameter tubes, but this was not always observed for atoms diffusing by a single-file mechanism in the smallest diameter tubes. This effect arises because the mixture density was maintained constant for a given composition for all diameters of CNTs.

For Ar/Ne mixtures ($\sigma_{\text{Ar}} = 0.342$ nm, $\sigma_{\text{Ne}} = 0.279$ nm) of given composition, for example, the number of molecules in the (7,7) CNT must be greater than that in the (6,6) nanotube, to maintain the same mixture density. However, although the accessible volume for the (7,7) nanotube is larger than for the (6,6), the Ar molecules can still only move in single-file and so are more tightly packed in the axial direction, leading to slower diffusion in the (7,7) tube (see Figs. 3.2(a), (c), and (e)). The same effect occurs for Ar/Xe mixtures ($\sigma_{\text{Ar}} = 0.342$ nm, $\sigma_{\text{Xe}} = 0.410$ nm), with Xe diffusing faster in the (6,6) nanotube than in the (7,7) and (8,8) nanotubes.

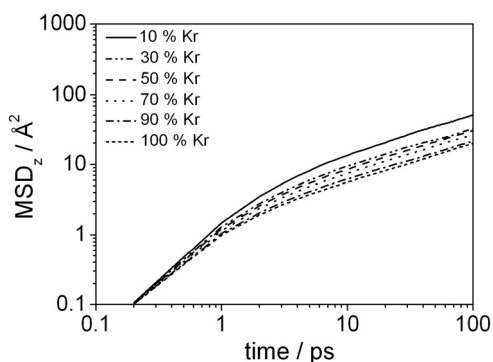
In all three mixtures, Ar diffused by a single-file mechanism in the (6, 6) and (7, 7) CNTs, with geometric diameters of 0.812 and 0.948 nm, respectively (Fig. 3.2(a), 3.2(c) and 3.2(e)). In larger diameter CNTs (with at least a 1.08 nm geometric diameter corresponding to the (8,8) CNT), Ar diffused by a Fickian mechanism. We refer to the maximum diameter CNT for single-file diffusion and the minimum diameter for Fickian diffusion as the “transition” diameters (*e.g.* (7,7) and (8,8) CNTs were the transition diameters for Ar). Hence, in Fig. 3.2(b), the transition diameters for Ne were the (6,6) and (7,7) CNTs. The transition diameters for Kr in Fig. 3.2(d) were the (7, 7) and (8, 8) CNTs, and for Xe in Fig. 2(f), they were the (8, 8) and (9, 9) CNTs.



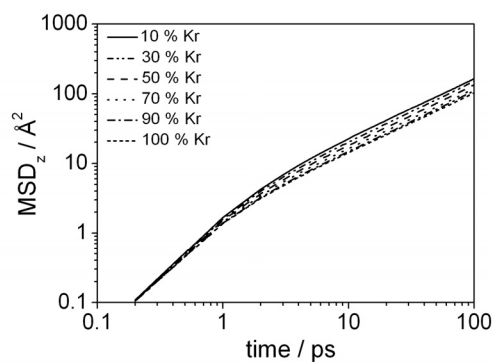
(a) Ne in Ar/Ne in (6,6) CNT



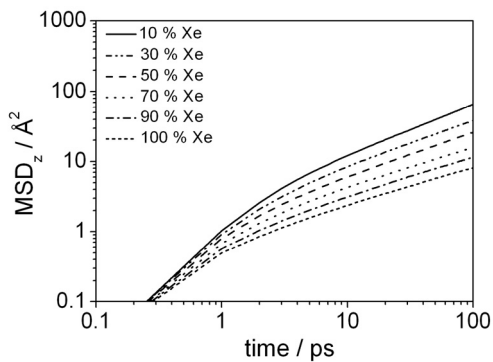
(b) Ne in Ar/Ne in (7,7) CNT



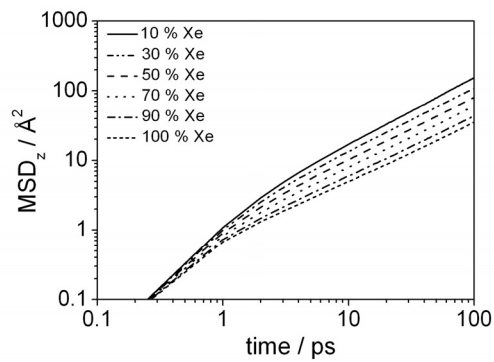
(c) Kr in Ar/Kr in (7,7) CNT



(d) Kr in Ar/Kr in (8,8) CNT



(e) Xe in Ar/Xe in (8,8) CNT



(f) Xe in Ar/Xe in (9,9) CNT

Figure 3.3: Axial direction mean squared displacements (MSDs) for Ne, Kr, and Xe in the transition diameter CNTs at 298 K.

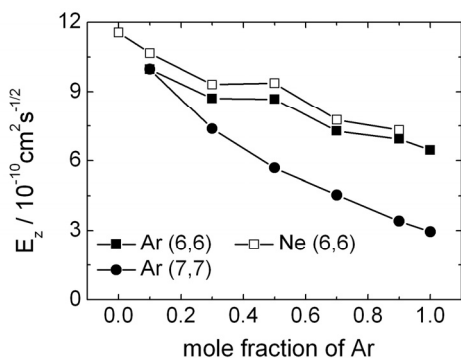
MSDs for Ne, Kr, and Xe are shown for the nanotubes at the transition diameters in Fig. 3.3 for compositions varying from 10 % to 100 % of each component in the mixture. From Fig. 3.3 we note that the diffusion mechanism for each component does not vary as a function of composition. In Fig. 3.3(a), Ne in the (6,6) CNT diffused by a single-file mechanism with the MSD proportional to the square root of time at all compositions, and it diffused by a Fickian mechanism in the (7,7) CNT (Fig. 3.3b) with the MSD proportional to time at all compositions. Likewise, Kr, at all compositions, diffused by a single-file mechanism in the (7,7) CNT (Fig. 3.3c) but by a Fickian mechanism in the (8,8) CNT (Fig. 3.3d). Xe, at all compositions, diffused by a single-file mechanism in the (8,8) CNT (Fig. 3.3e) and by a Fickian mechanism in the (9,9) CNT (Fig. 3.3d). All of the slopes on the log-log plots of the MSD in Fig. 3.3 are observed to be 1/2 for the single-file diffusing tubes (Figs. 3.3(a), 3.3(c), and 3.3(e)) and 1 for the Fickian diffusing tubes (Figs. 3.3(b), 3.3(d), 3.3(f)). Any variations are likely due to finite size effects previously discussed^{27, 29}.

Ne in the Ar/Ne mixture (Figs. 3.3a and 3.3b) diffused faster with increased composition of Ne, but Kr (Figs. 3c and 3d) and Xe (Figs. 3.3e and 3.3f) diffused faster with decreased composition. This was the result of the lighter component in each mixture diffusing faster. Thus, Ne ($MW_{\text{Ne}} = 20.18 \text{ g/mol}$) is lighter than Ar ($MW_{\text{Ar}} = 39.95 \text{ g/mol}$), and Ne diffused faster with decreased composition of Ar. Kr ($MW_{\text{Kr}} = 83.80 \text{ g/mol}$) and Xe ($MW_{\text{Xe}} = 131.29 \text{ g/mol}$) are both heavier than Ar, and their diffusional rate decreased with decreased composition of the heavier component.

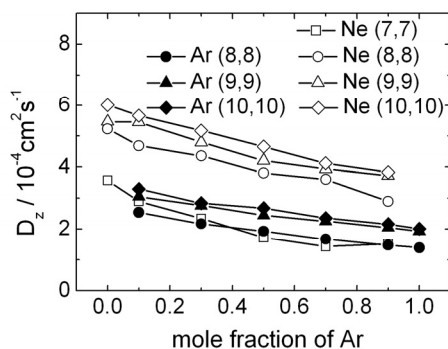
3.3.2 Diffusion Coefficients

Self-diffusion coefficients for each component in each mixture as a function of Ar mole fraction are shown in Fig. 3.4. In Fig. 3.4(a), 3.4(c) and 3.4(e), the single-file mobilities are reported, while in Fig. 3.4(b) 3.4(d) and 3.4(f), Fickian diffusion coefficients are reported. Single-file mobilities due to the dependence of the MSD on the square root of time are shown with units of $\text{cm}^2/\text{s}^{1/2}$, while the Fickian diffusion coefficients are reported with units of cm^2/s due to the linear time dependence of the MSD. The single-file mobilities (Fig. 3.4a) and Fickian diffusion coefficients (Fig. 3.4b) decreased with increased composition of Ar in the Ar/Ne mixture. This was a direct result of Ne being lighter than Ar, as previously discussed in terms of the MSDs. Similarly in the Ar/Kr and Ar/Xe mixtures, the single-file mobilities and Fickian diffusion coefficients increased with increased composition of Ar, due to Kr or Xe being heavier.

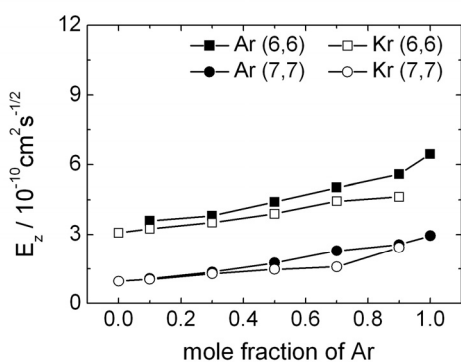
The coefficients in Fig. 3.4 were fitted according to Eqn. 3.1 for Fickian diffusion and Eqn. 3.2 for single-file diffusion. We have fitted the time dependence of the MSD to be 1 (according to Eqn. 2.3) for the Fickian diffusion coefficients and 1/2 for the single-file mobilities (according to Eqn. 2.4). The best fitted values of this regression are shown in Fig. 3.4. Error bars are not shown for clarity, but those which extend 1.96 times the standard error of the fitted coefficients (a 95 % confidence interval) were $\sim 5 \times 10^{-11} \text{ cm}^2/\text{s}^{1/2}$ for the single-file mobilities and $\sim 5 \times 10^{-5} \text{ cm}^2/\text{s}$ for the Fickian diffusion coefficients. Thus, while in



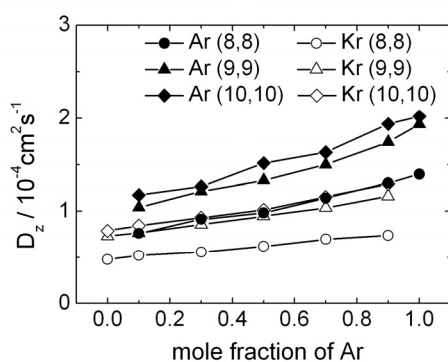
(a) Single-file mobilities in Ar/Ne mixtures



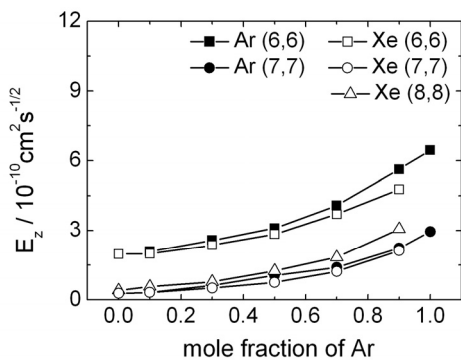
(b) Diffusivities in Ar/Ne mixtures



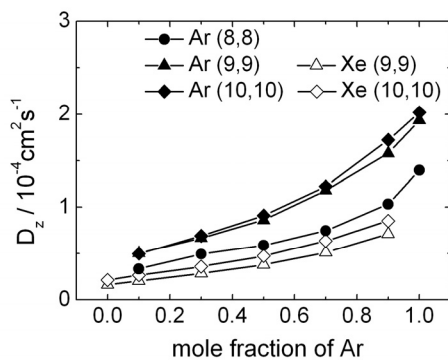
(c) Single-file mobilities in Ar/Kr mixtures



(d) Diffusivities in Ar/Kr mixtures



(e) Single-file mobilities in Ar/Xe mixtures



(f) Diffusivities in Ar/Xe mixtures

Figure 3.4: Axial direction single-file mobilities (a,c,e) and Fickian self-diffusion coefficients (b,d,f) for Ne, Ar, Kr, and Xe in Ar/Ne, Ar/Kr and Ar/Xe mixtures at 298 K in the indicated CNTs.

the same diameter CNT, Ne appears to diffuse faster than Ar at all compositions, statistically the error bars overlap. A similar observation can be made for the error bars associated with the Ar/Kr and Ar/Xe mixtures.

As observed for the MSDs in section 3.3.1, the single-file mobilities for components that diffused in the (6,6) CNTs were faster than in the (7,7) CNTs due to our comparison of the same density at each composition. Otherwise, the diffusion coefficients increased with increased diameter of the CNT.

Recently, experimental evidence has been presented which shows a transition from single-file to Fickian diffusion. Das *et al.*¹⁵ have reported experimental results for water diffusing in single-file in 1.4 nm single-walled carbon nanotubes using PFG-NMR. They observed a clear transition from single-file to Fickian diffusion as the temperature was increased from 271 K to 298 K. Between 228 K and 271 K, water molecules near the wall of the CNT were frozen and immobile, but a single-file chain of water near the center of the CNT were mobile and diffused in single-file. As the temperature was increased from 271 K to 298 K, the effective pore diameter, where diffusion of mobile water molecules occurred, increased, and the diffusion was observed to transition from a single-file mode at 271 K to a Fickian mode at 298 K. Secondly, at the lower temperatures where single-file diffusion was reported, the immobile water molecules near the CNT wall could have contributed to an effective corrugated surface, allowing the chain of single-file water to exhibit the needed

random walk and thus the exhibited square-root of time dependence of the mean-squared displacement. However, we also point out that there are many other effects that could contribute to the corrugation of the pore including atomic defects in the carbon nanotube wall as well as bends, junctions and other orientational defects⁴⁷. Thus the models of CNTs we have presented with effective corrugated walls using a stochastic thermostat is an attempt to mimic the combined effect of these defects.

3.4 Conclusion

Carbon nanotube structures provide a means to systematically investigate the diffusion mechanism of simple Lennard-Jones fluid mixtures under confinement. We have used a stochastic thermostat within these carbon nanotube structures to provide models of tubes with effective corrugated walls, to model the random walk of particles diffusing in three-dimensions (Fickian diffusion) and one-dimension (single-file diffusion) within cylindrical pores. The random walk within cylindrical pores has been shown to be needed to give rise to the square root of time dependence of the mean-squared displacement (MSD) for single-file diffusion².

Within this framework we showed that for Lennard-Jones mixtures, transition diameters of carbon nanotubes (CNTs) existed for each component, the crossover from single-file to Fickian self-diffusion occurring at $D \sim 2.6\sigma - 2.8\sigma$, measured geometrically with respect to the largest component in the mixture. For Ar and Kr the transition diameter CNTs were the

(7,7) CNT which gave rise to single-file diffusion, where the mean-squared displacement was proportional to the square root of time and the (8,8) CNT which gave rise to Fickian diffusion, where the mean-squared displacement was proportional to time. For Ne, the (6,6) CNT gave rise to single-file diffusion while the (7,7) and larger diameter CNTs gave rise to Fickian diffusion. For Xe, the (6,6), (7,7), and (8,8) CNTs gave rise to single file diffusion while CNTs larger in diameter gave rise to Fickian diffusion. The diffusion mechanism (single-file or Fickian) did not depend on the composition of the mixture.

Of particular interest was that for both Ar/Ne ($\sigma_{\text{Ar}}/\sigma_{\text{Ne}} = 1.23$) and Ar/Xe ($\sigma_{\text{Xe}}/\sigma_{\text{Ar}} = 1.20$) mixtures, it was possible to choose nanotube diameters ((7,7), $d_T = 0.948$ nm for Ar/Ne, (8,8), $d_T = 1.08$ nm for Ar/Xe) so that the large molecules (Ar in the first case, Xe in the second) diffused in single-file mode, while the smaller ones were able to diffuse in the very much faster Fickian mode. For Ar/Kr mixtures, by contrast ($\sigma_{\text{Kr}}/\sigma_{\text{Ar}} = 1.06$) it was not possible to find a nanotube whose diameter permitted such bimodal diffusion.

CHAPTER 4

Dual-Mode Diffusion of Argon Confined within Single-Walled Carbon Nanotube Bundles

4.1 Introductionⁱ

In Chapters 2 and 3, the diffusion of Lennard-Jones fluids were investigated in isolated single-walled carbon nanotubes. A square root of time dependence of the mean-squared displacement was observed, but as we described, this was a result of a mimicked surface corrugation, which is needed to observe anomalous diffusion in single-file^{2, 27}. For argon adsorbed in single-file in isolated carbon nanotubes, this effect is shown in more detail in an appendix 4A to this chapter. There we show that microcanonical molecular dynamics simulations give rise to a size correlation effect, as was observed by Hahn and Kärger^{27, 28} and illustrated in Chapter 1. We also show additional effects due to drifts in the center of mass. These drifts lead to collective motion of the fluid in single-file, which has previously been seen for water³¹ in carbon nanotubes and described to be a result of strong hydrogen bonding effects. With argon, there is of course no hydrogen bonding, and this collective motion is purely an artifact of the simulation due to numerical imprecision caused by the

ⁱ Material from this chapter has been published in Y.C. Liu*, J.D. Moore*, T.J. Roussel, and K.E. Gubbins, "Dual Diffusion Mechanism of Argon Confined in Single-Walled Carbon Nanotube Bundles", *Physical Chemistry Chemical Physics*, 12, 6632-6640 (2010). Reprinted with permission from The Royal Society of Chemistry, Copyright (2010).

*Equal Contribution

inherent one-dimensional aspect of single-file diffusion. For simulations with small system sizes, it is difficult to adequately sample enough of the Maxwell-Boltzmann distribution of velocities, especially in a quasi-one dimension (such as Fickian diffusion in a carbon nanotube) and especially in one-dimension (such as single-file diffusion in a carbon nanotube). By performing molecular dynamics simulations with adequate system sizes, these effects are greatly diminished and more accurate estimates of the diffusion properties are obtained. In this chapter, we illustrate this effect for the case of argon diffusing in a (25,0) carbon nanotube bundle.

For an atomically detailed model of a cylindrical pore (such as a single-walled carbon nanotube) the momentum exchange between fluid atoms and wall atoms during collisions is expected to be important, especially at low pressure⁴⁸. To account for this momentum exchange, we can think of three possible routes. The first is to include corrugations to the pore in some *ad hoc* manner such as a sinusoidal fluid-wall potential. However for light gases diffusing in single-walled carbon nanotubes, the reflections are nearly specular³⁴ indicating very little corrugation seen by all but the smallest atoms. The second is to model a fully flexible wall, which is computationally demanding. The third route is the inclusion of random forces (for example randomly altering the velocities at some interval). This can be accomplished in an *ad hoc* manner which would not necessarily guarantee sampling a true thermodynamic ensemble or yield the rigorously correct dynamics (similarly to simple velocity rescaling). A more rigorous way would be through the inclusion of a thermostat

which includes some random term (*e.g.*, a friction term), but these thermostats do not guarantee the sampling of the correct dynamics because the stochastic collisions of the atoms lead to a decorrelation of their velocities⁴⁹. Possible thermostats to attempt to approximate the fluid-wall momentum exchange are the Langevin^{50, 51} (as was used in Chapters 1 and 2), Berendsen⁵², and Andersen⁵³ thermostats.

Recently a thermostat based upon the Andersen scheme was proposed by Keil and co-workers⁵⁴ to account for this fluid-wall momentum exchange. The Lowe-Andersen thermostat mimics fluid-wall momentum exchange by modifying velocities based upon frequencies which are fitted to fully flexible simulations. Keil and co-workers^{48, 54} found for fluids in carbon nanotubes with diameters that exhibited Fickian diffusion, modification of their velocities based upon these fitted frequencies for rigid carbon nanotubes reproduced the diffusion coefficients from fully flexible simulations. A rigid tube without this thermostat produced too high a diffusion coefficient at low pressure (at high pressure the influence of flexibility seemed to be negligible).

Here, we examine a (25,0) carbon nanotube bundle, which should be a more realistic model of a carbon nanotube system compared to isolated carbon nanotubes. The inner channels of the carbon nanotube are large enough to result in Fickian diffusion of argon, while the interstices between the carbon nanotubes provide pores large enough to adsorb argon but small enough to restrict the diffusion in single-file. As the interstitial sites are

composed of the outside walls of the nanotubes, they are naturally corrugated. Thus fluid atoms diffusing in these interstitial sites are expected to exhibit a random walk and the anomalous $t^{1/2}$ dependence of the mean-squared displacement. The adsorption⁵⁵ of fluids in carbon nanotube bundles has been studied, but to our knowledge previous diffusional studies⁵⁶ have not examined multi-modal diffusion mechanisms with atoms diffusing in single-file in the interstices. This is likely due to artifacts of the simulation due to system size effects, which we examine in detail. Dynamic properties are measured from microcanonical simulations to prevent influences of stochastic collisions and decorrelated velocities. We also investigate the influence of the carbon nanotube flexibility and loading on the diffusion of argon.

4.2 Computational Methods

We have employed Grand Canonical Monte Carlo (GCMC) simulations to compute isotherms of argon at 120 K in infinitely long (25,0) carbon nanotube bundles, allowing adsorption in both the SWCNTs and in interstices between the SWCNTs. We use molecular dynamics simulations (MD) to measure the self-diffusivity of argon in the SWCNT bundles. The geometric structure of these defect free SWCNT bundles has been previously defined⁵⁷. Our unit cells consist of four nanotubes with periodic boundary conditions. The interlayer distance between graphene layers in graphite is 0.335 nm⁵⁸. When these graphene sheets are rolled up to form carbon nanotube bundles, the distance between the nanotubes increases

with decreasing carbon nanotube diameter, and has been experimentally measured⁵⁹. To account for this increase, the nanotubes in this study are separated by 0.35 nm (larger than in graphite) which is hexagonally distributed. This provided interstitial sites with a geometric diameter of 0.819 nm, which was small enough to give rise to single-file diffusion for argon and which we have shown previously for narrow isolated carbon nanotubes⁵¹. The inner channels of the SWCNTs had a geometric diameter of 1.954 nm and gave rise to Fickian diffusion for argon.

4.2.1 Grand Canonical Monte Carlo Simulations

Grand Canonical Monte Carlo (GCMC) simulations were used to compute the adsorption isotherm of argon at 120 K in a rigid (25,0) SWCNT bundle. The GCMC method simulates the chemical equilibrium reached between a fictitious gas reservoir containing bulk argon and the adsorbed argon phase in the carbon structures by constraining the chemical potential of the two phases to be equal. The bulk argon phase was treated as an ideal gas under the state conditions examined in this study, which allowed for the chemical potential and pressure of the bulk phase to be related using the ideal gas equation of state. The difference between the absolute amount adsorbed as calculated using GCMC and the excess amount adsorbed as would be measured experimentally was negligible under the examined state conditions. Thus, no additional corrections were applied to the simulated isotherms. For each state point, the system was equilibrated using a minimum of 2.5×10^8 Monte Carlo trials, followed by an additional 2.5×10^8 trials over which statistics were collected. Each

Monte Carlo trial consisted of an attempted translation, insertion or deletion of an argon molecule. The final argon configurations were used as the initial configurations for the simulations at subsequent state points in the isotherms. Both argon and carbon were modeled as a simple Lennard-Jones fluid with $\varepsilon_{Ar}/k_B = 124.07\text{ K}$ and $\sigma_{Ar} = 0.342\text{ nm}$ and $\sigma_C = 0.340\text{ nm}$ and $\varepsilon_C/k_B = 28.00\text{ K}$ for argon⁴⁰ and carbon⁴¹, respectively. The parameters for the argon-carbon interaction parameters were estimated using the Lorentz-Berthelot mixing rules, $\sigma_{ij} = (\sigma_i + \sigma_j)/2$ and $\varepsilon_{ij} = \sqrt{\varepsilon_i \varepsilon_j}$, to yield $\sigma_{Ar-C} = 0.341\text{ nm}$ and $\varepsilon_{Ar-C}/k_B = 58.94\text{ K}$. A cutoff of 12 \AA was used for the potentials. The unit cell periodic lengths were 4.5789 nm , 3.9655 nm , and 5.5302 nm in the x,y, and z directions, respectively, with the axial tube lengths in the z direction. Periodic boundary conditions were applied to the unit cells in all three directions and the pair-wise interactions were evaluated using the minimum image convention. Prior to the start of the simulations, the argon-carbon interactions were calculated at 8×10^6 evenly spaced grid points that divided the unit cell containing the carbon structure. These values were then stored and used during simulations to calculate the argon-carbon interactions throughout the unit cell of the carbon structure using a linear interpolation scheme to estimate the energy between grid points.

4.2.2 Molecular Dynamics Simulations

Molecular dynamics (MD) simulations were used to measure the self-diffusivity of argon inside the SWCNT bundles. The same potentials and parameters that were used in the

GCMC simulations were used in the MD simulations. A cutoff of 12 Å was also used for the potentials except that in the MD simulations a smoothing function was utilized from 10 Å to 12 Å, allowing for both the energy and the force of the LJ potential to smoothly go to zero without any discontinuities. This smoothing function is commonly used in many MD packages including GROMACS⁶⁰ (GRONingen Machine for Chemical Simulations) and NAMD⁴³ (Nanoscale Molecular Dynamics) to prevent discontinuities. All of our MD simulations have been performed with the LAMMPS (Large-scale Atomic/Molecular Massively Parallel Simulator) simulation package⁶¹. The final configurations from the GCMC simulations were used as the starting configurations in the MD simulations. Each system was replicated at least 5 times along the axial z direction to obtain better statistics for the mean squared displacement and to investigate system size effects. In all of the simulations, the equations of motion were integrated using the velocity-Verlet algorithm, with an integration timestep of 1 femtosecond (fs). At the start of the simulations velocities were randomly chosen for each fluid atom from a Maxwell-Boltzmann distribution centered at 120 K, the total linear and angular momenta of the fluid were zeroed, and the velocities were rescaled to yield a temperature of 120 K.

Each MD simulation was equilibrated at 120 K using a Nosé-Hoover thermostat with a damping coefficient of 0.001 ps for 1 ns followed by a microcanonical (NVE) production run of at least 10 ns. Saved trajectories (spaced at 0.5 ps) from the microcanonical productions were used to calculate the mean squared displacement using multiple time origins every 25

ps. Temperature fluctuations in the microcanonical simulations were generally less than 2 K and the total energy varied less than 0.1 %. As in the GCMC simulations, periodic boundary conditions were applied to the unit cells and pair-wise interactions were evaluated using the minimum image convention.

In the MD simulations, we have used both rigid and flexible SWCNT bundles. In the case of the flexible bundle, the C-C intramolecular interactions were defined with the potential of Walther *et al.*⁶², which uses a Morse potential for the bond, a harmonic cosine, and a 2-fold torsion potential:

$$\begin{aligned}
 U(r_{ij}, \theta_{ijk}, \phi_{ijkl}) = & K_{Cr} \left(1 - \exp(-\gamma(r_{ij} - r_c)) \right)^2 \\
 & + \frac{1}{2} K_{C\theta} (\cos \theta_{ijk} - \cos \theta_C)^2 \\
 & + \frac{1}{2} K_{C\phi} (1 - \cos 2\phi_{ijkl})
 \end{aligned} \tag{4.1}$$

In Eq. (4.1), the first term represents the carbon-carbon bonds and has the parameters $K_{Cr} = 478.9 \text{ kJ mol}^{-1}$, $r_c = 1.418 \text{ \AA}$, and $\gamma = 2.1867 \text{ \AA}^{-1}$. The second term represents carbon's bond angles and has the parameters $K_{C\theta} = 562.2 \text{ kJ mol}^{-1}$ and $\theta_C = 120.00^\circ$. The last term represents carbon's torsional angles and has the parameter $K_{C\phi} = 25.12 \text{ kJ mol}^{-1}$. This model has previously been used by Keil and coworkers to compare the diffusion of fluids in isolated rigid carbon nanotubes with flexible ones from very low to high pressures

and was used as the basis for their previously described Lowe-Andersen thermostat^{48, 54}. We are modeling infinitely long SWCNTs in both the rigid and flexible cases. Thus, our flexible models allow for all of the carbon atoms to move, and bonds, bond angles, and torsional angles are modeled across the periodic boundaries, where the minimum image convention was used to evaluate the distances. In both the rigid and flexible simulations, carbon-carbon Lennard-Jones interactions were not taken into account within the same SWCNT, which we found (and has previously been described⁴⁸) not to have an effect on the diffusion of fluids inside carbon nanotubes. However, for the flexible SWCNT bundle simulations we did account for Lennard-Jones carbon-carbon interactions between carbons in different SWCNTs. This prevented the SWCNTs from unrealistically drifting apart. In the flexible bundles, as with the rigid bundles, the simulations were prepared by first selecting random velocities from a Maxwell-Boltzmann distribution and then zeroing the total linear and angular momenta of the fluid. The momenta of the carbon was zeroed separately, and thus the entire system's momenta were zero. The equilibration and production runs were performed in the same manner as previously described.

4.3 Results and Discussion

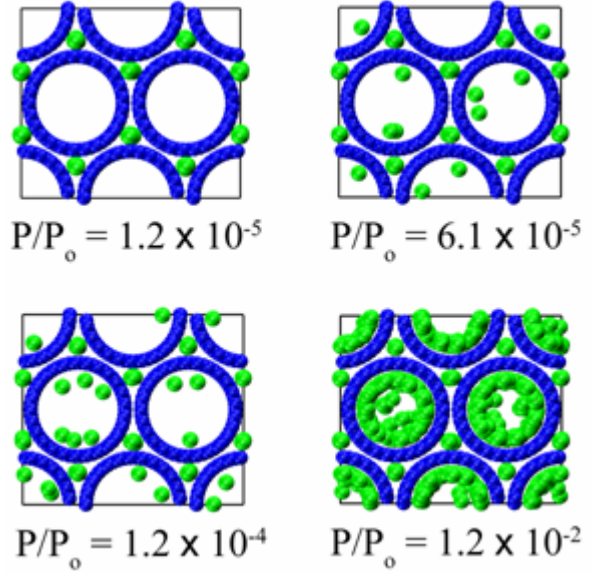
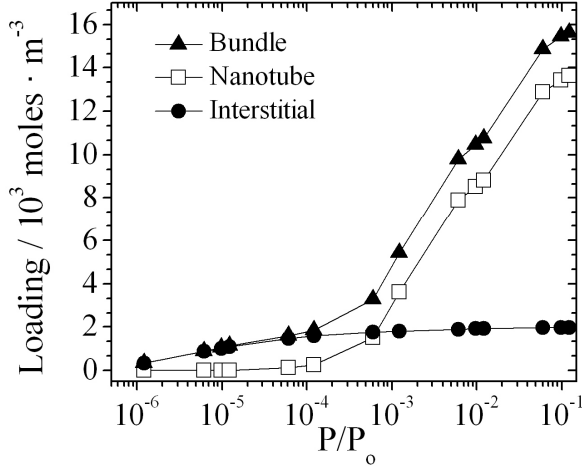
4.3.1 Adsorption Isotherm

In the (25,0) SWCNT bundle, the pore size distribution is bi-modal and includes small interstitial sites which we show later in the article give rise to single-file diffusion of

argon. Larger channels within the (25,0) SWCNTs give rise to Fickian diffusion for argon. In Fig. 1(a) we show the adsorption isotherm for argon in the rigid (25,0) SWCNT bundle. In Fig. 1(a), the pressure, P , was normalized by the vapor pressure, P_0 , of argon at 120 K which was measured from the Lennard-Jones equation of state⁶³ as 8.2 bar using the parameters in this study. As the SWCNT bundle's structure is exactly known geometrically, we were able to isolate the adsorption of argon atoms in the interstitial sites from those in the nanotubes. Thus in Fig. 4.1(a) we show the total isotherm due to the collective fluid (Bundle) for argon as well as the isotherms of the nanotube and interstitial argon atoms. Argon is first adsorbed in the interstitial sites until $P/P_0 \sim 6.1 \times 10^{-5}$ above which argon starts to adsorb in the nanotubes. Above this pressure, the interstitial sites are almost completely filled and further adsorption occurs appreciably only in the nanotubes. Atoms first adsorb in the nanotubes along the surface in a monolayer until $\sim P/P_0 \sim 10^{-2}$ when the nanotubes start to fill with adsorbent. In Fig. 4.1(b) we show GCMC snapshots at various pressures which illustrate this filling.

4.3.2 Diffusion Mechanisms

In Fig. 4.2 we show the mean squared displacements (MSDs) at various relative pressures for argon diffusion in the (25,0) SWCNT bundle at 120 K. The results shown are for system sizes which utilized $\sim 10,000$ interstitial atoms at each pressure. This was to overcome size correlation effects for single-file diffusion previously described by Hahn and



(a)

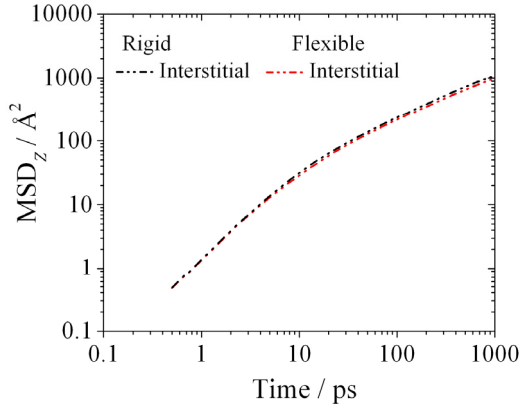
(b)

Figure 4.1: Loading of argon in a (25,0) SWCNT bundle as a function of relative pressure (P/P_0) at 120 K. (a) Adsorption isotherms for all of the atoms in the total bundle (triangles), for only the atoms within the nanotubes (squares) and interstitial adsorbed atoms (circles); (b) snapshots from GCMC simulations at 120 K corresponding to the relative pressures indicated.

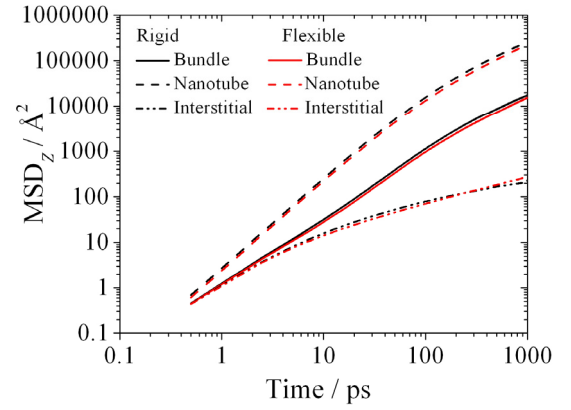
Karger²⁷ and which we have observed in our simulations. All three diffusion mechanisms (ballistic, Fickian and single-file) are seen in our simulations. At sub-picosecond time scales the MSDs exhibit ballistic motion with the slope of the MSD versus time on the log-log scale equal to 2. At the lowest pressure in Fig. 4.2(a) where $P/P_0 = 1.2 \times 10^{-5}$, there were no argon atoms adsorbed in the inner channels of the SWCNTs, and thus the total MSD is that for the interstitial atoms and is observed to obey a square root of time dependence at times greater than ~ 100 ps. As the pressure was increased, argon atoms began to adsorb in the nanotubes,

where the mean-squared displacement was observed to obey a linear time dependence for times greater than ~ 100 ps. The argon atoms in the interstitial sites again were observed to obey a square root of time dependence for times greater than ~ 100 ps. The total MSD (which accounted for all of the fluid atoms in the system) obeyed a linear time dependence, since the diffusion of argon atoms in the nanotubes is orders of magnitude faster than those in the interstitial sites. Thus the total MSD of the collective fluid in the bundle approached that of the nanotube argon atoms as the pressure was increased.

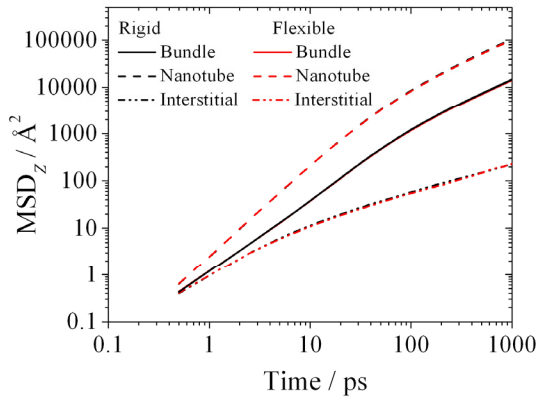
Fig. 4.2 also shows a comparison between rigid and flexible SWCNT bundles. For the system sizes indicated in Fig. 4.2, only a small effect of the SWCNT flexibility was observed at $P/P_o = 1.2 \times 10^{-5}$ where only interstitial argon atoms were present and at $P/P_o = 6.1 \times 10^{-5}$ where nanotube channel argon atoms first began to adsorb. At higher pressures very little effect of the SWCNT flexibility was observed for argon atoms diffusing in the nanotubes or in the total bundle. At $P/P_o = 1.2 \times 10^{-4}$, there was no noticeable effect of the flexibility for the interstitial atoms. At the highest pressure, $P/P_o = 1.2 \times 10^{-2}$, while there appears to be good agreement between the rigid and flexible nanotube and total bundle MSDs, the interstitial MSD shows significant disagreement. We attribute this to an inadequate system size, which may also still be suffering from the size correlation effects observed by Hahn and Karger²⁷ and that we have seemingly overcome at lower pressure. At $P/P_o = 1.2 \times 10^{-2}$ we have utilized a system size of 9,360 interstitial argon atoms and 42,320 inner channel argon atoms. While modeling a larger number of argon atoms is achievable in



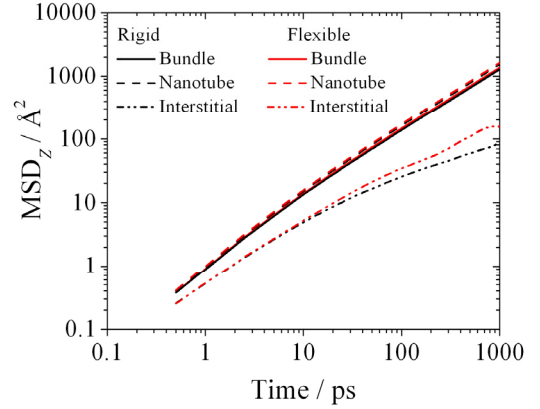
(a) $P/P_o = 1.2 \times 10^{-5}$



(b) $P/P_o = 6.1 \times 10^{-5}$



(c) $P/P_o = 1.2 \times 10^{-4}$



(d) $P/P_o = 1.2 \times 10^{-2}$

Figure 4.2: Mean squared displacement of argon along the axial direction of (25,0) rigid (black) and flexible (red) SWCNT bundles in the nanotubes (dashed), interstitial sites (dashed-dot), and total bundle (line) at 120 K and various relative pressures (P/P_o). System sizes varied by pressure but $\sim 10,000$ interstitial argon atoms were used in each case. In (a) $P/P_o = 1.2 \times 10^{-5}$: there are 10,064 interstitial argon atoms in the simulation and no argon atoms in the nanotubes; in (b) $P/P_o = 6.1 \times 10^{-5}$: there are 10,080 interstitial and 728 nanotube argon atoms; in (c) $P/P_o = 1.2 \times 10^{-4}$: there are 11,820 interstitial and 1,860 nanotube argon atoms; in (d) $P/P_o = 1.2 \times 10^{-2}$: there are 9,360 interstitial and 42,320 nanotube argon atoms.

the rigid model, the modeling of the flexible SWCNT bundles themselves is the computational barrier, as this system requires modeling the flexibility of 416,000 carbon atoms. Our goal in Fig. 4.2 is to compare rigid and flexible structures at the same system size, and therefore we have not shown a larger system size for $P/P_o = 1.2 \times 10^{-2}$ due to the computational burden of modeling a larger flexible SWCNT bundle.

In Fig. 4.3 we show the diffusion coefficients for argon calculated from the linear regions of the MSDs in Fig. 4.2. The diffusion coefficients are fit according to Eq. (1.1) for the nanotube atoms and total bundle and to Eq. (1.2) for the interstitial sites. In calculating the diffusion coefficients we have fitted the time dependence of the MSDs for the nanotube and total bundle atoms to have a slope (on the log-log scale of the MSD as a function of time) of 1 (according to Eq. (1.1)) and 1/2 (according to Eq. (1.2)) for the interstitial single-file mobility (F). The best-fit values of the diffusion coefficients from this regression are shown as symbols in Fig. (4.3), while the error bars shown are extended 1.96 times the standard error of the fitted diffusion coefficients. Thus, the error bars represent the 95 % confidence interval of the fitted diffusion coefficients.

As observed in Fig. 4.2 for the MSDs at $P/P_o = 1.2 \times 10^{-5}$, where only interstitial atoms are present in the bundle, there is only a small difference in the single-file mobilities for the rigid and flexible cases. As the pressure is increased further, the fitted single-file mobilities for the rigid and flexible simulations have overlapping error bars. The error bars for the

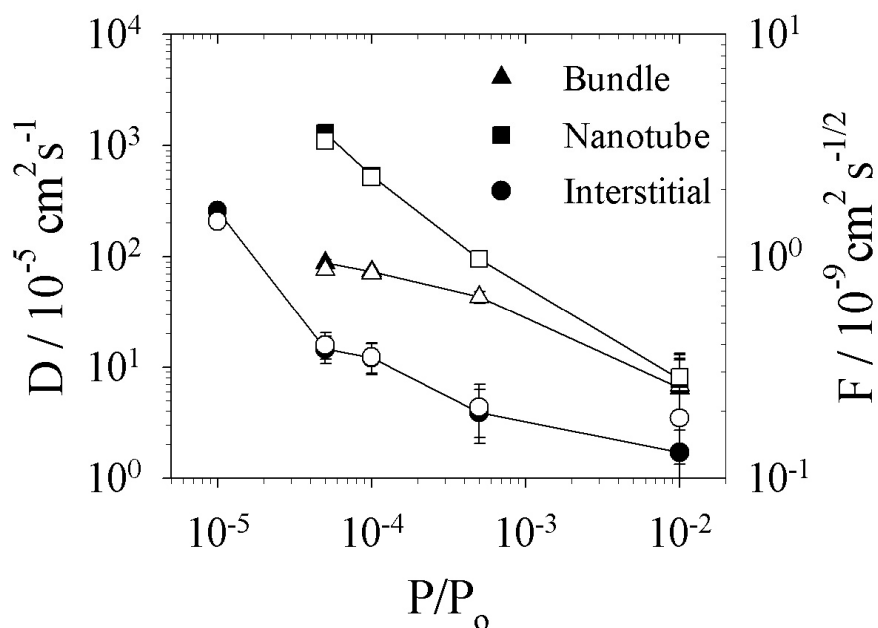


Figure 4.3: Self-diffusion coefficients for argon diffusing in a rigid and flexible (25,0) SWCNT bundle as a function of relative pressure. The argon atoms in the nanotubes (squares) as well as the total bundle (triangles) exhibit Fickian diffusion and their y-axis is shown on the left. The argon atoms in the interstitial sites (circles) exhibit single-file diffusion and their y-axis is shown on the right. Solid symbols indicate a rigid SWCNT bundle while open symbols indicate a flexible SWCNT bundle. Lines are shown as a guide for the eye.

lowest pressures in Fig. 4.3 are smaller than the symbols. However, with increasing pressure the fits are poorer for the single-file mobilities and the error bars increase. The fitted diffusion coefficients, D , for argon in the nanotubes and total bundle also show small differences between the rigid and flexible simulations at $P/P_o = 6.1 \times 10^{-5}$, where atoms are first adsorbed in the nanotubes. As the pressure is increased the error bars also increase, but to a much smaller degree than was observed for the single-file mobilities in the interstitial sites. The fitted diffusion coefficients for the rigid and flexible SWCNTs have overlapping

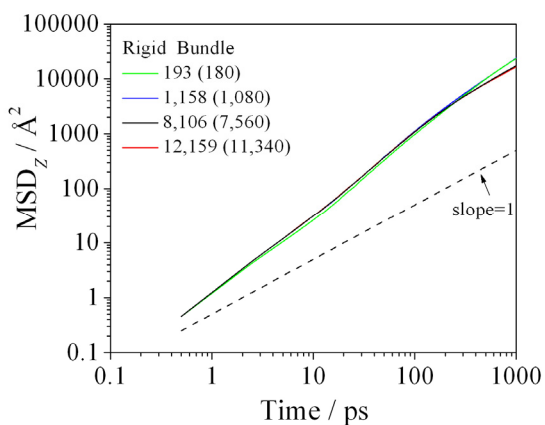
error bars in all cases. For both the single-file mobilities for the single-file diffusing atoms in the interstitial sites and the Fickian self-diffusion coefficients for the atoms in the nanotubes and total bundle, the error for the highest pressure studied, $P/P_o = 1.2 \times 10^{-2}$, is the largest.

4.3.3 System Size Effects in Flexible and Rigid Bundles

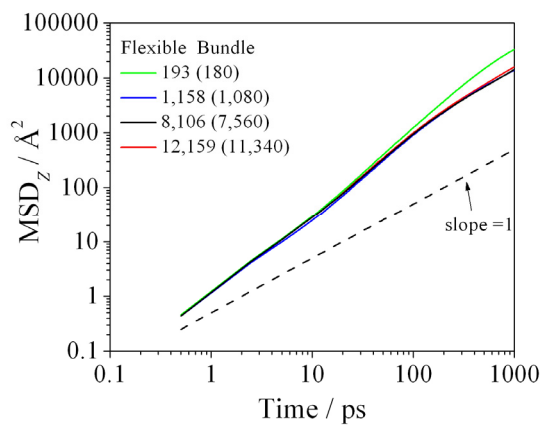
In Figs. 4.2 and 4.3 we have shown a very small effect of the flexibility of the SWCNT bundle on argon diffusion, even at the lowest pressures studied. The influence of flexibility on the diffusion of fluids inside carbon nanotubes has drawn considerable attention^{34, 48, 54, 55, 64-70}, and there are still controversies on this topic. Marmier *et al.* calculated the self-diffusivities of argon atoms diffusing through SWCNTs⁶⁹. They found that the flexibility of the SWCNTs had no noticeable influence on the diffusivity of argon for the densities they studied. Keil and co-workers^{48, 54} and Chen *et al.*⁷⁰ reported that molecular dynamics simulations of fluids diffusing in flexible SWCNTs at low pressure produced diffusion coefficients that could be an order of magnitude smaller than for their corresponding rigid nanotube simulations. Many of these simulations used only tens or hundreds of fluid atoms. We find that for the diffusion of argon in (25,0) SWCNT bundles the system size (number of fluid atoms in the simulation) greatly influences the MSD and thus the diffusion coefficients. This is especially true for single-file diffusion within the interstitial channels.

In Fig. 4.4, we compare rigid and flexible nanotube simulations at various system sizes for the total bundle MSD and for the interstitial MSD at $P/P_o = 6.1 \times 10^{-5}$, the smallest pressure at which there was adsorption and diffusion of argon in both the interstitial and inner nanotubes. For the total bundle MSD for the rigid (Fig. 4.4(a)) and flexible (Fig. 4.4(b)) SWCNT bundles, system sizes less than $\sim 8,106$ total fluid atoms (7,560 interstitial atoms and 546 inner channel atoms) yield diffusion coefficients that are too large. Further increase in the system size to 12,159 total fluid atoms (11,340 interstitial and 819 nanotube channel atoms) shows nearly identical results to the 8,106 total fluid atom system size, thus indicating that we have achieved a system size large enough for diffusion inside the nanotubes. A greater dependence on system size is shown for the interstitial MSDs for the rigid (Fig. 4.4(c)) and flexible (Fig. 4.4(d)) SWCNT bundles. The single-file atoms diffusing in the interstitial channels have strong size correlations, as previously discussed by Hahn and Karger²⁷, . For the interstitial diffusing atoms, system sizes of at least 8,106 total fluid atoms appear to be needed at $P/P_o = 6.1 \times 10^{-5}$. Further increases in the system size show nearly identical results, indicating that we have achieved a system size that is large enough.

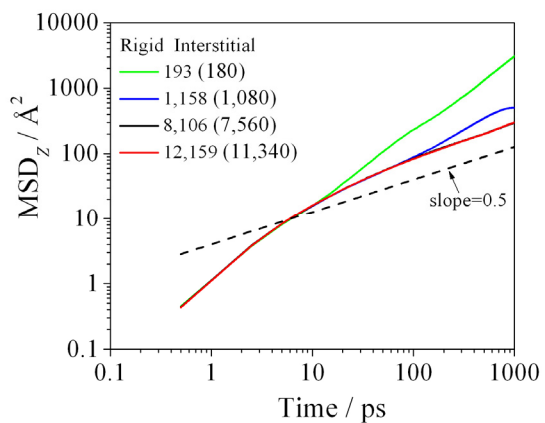
In Fig. 4.5, we compare simulation results for rigid and flexible nanotube bundle simulations at various system sizes for argon atoms in the total bundle MSD and the interstitial MSD at $P/P_o = 1.2 \times 10^{-2}$. For the total bundle MSD for the rigid (Fig. 4.5(a)) and flexible (Fig. 4.5(b)) SWCNT bundles, system sizes of at least 7,752 total fluid atoms (1,404 interstitial and 6,348 nanotube atoms) appear to be large enough, as further increases in the



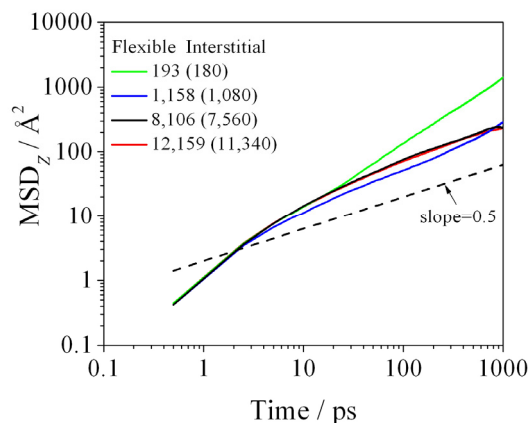
(a)



(b)

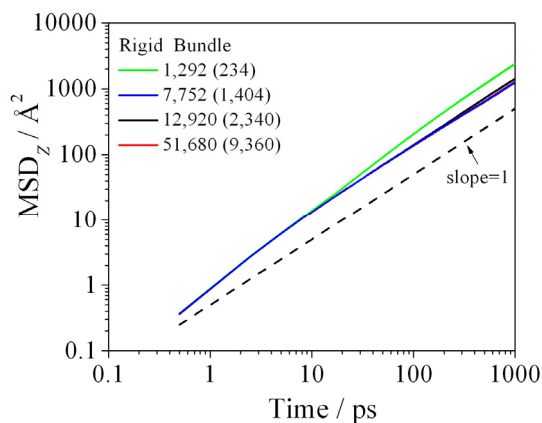


(c)

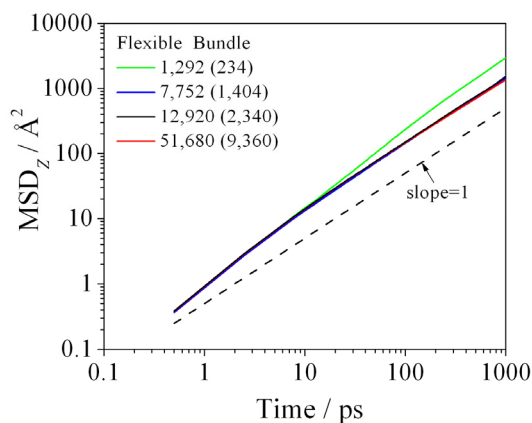


(d)

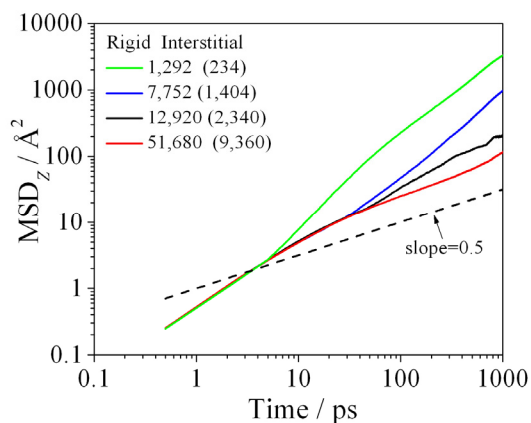
Figure 4.4: The effect of system size on the mean squared displacement as a function of the total number of argon atoms at $P/P_o = 6.1 \times 10^{-5}$. In (a) and (b) the MSD for argon atoms in the total bundle is compared for the rigid and flexible cases, respectively. In (c) and (d) the MSD for argon atoms in the interstitial sites are compared for the rigid and flexible cases, respectively. The numbers listed on the graphs indicate the total number of argon atoms in the simulation and those in the interstitial sites are in parenthesis. The dashed line illustrates the nominal slope expected for Fickian diffusion in (a) and (b) and single-file diffusion in (c) and (d) with slopes of 1 and $1/2$, respectively.



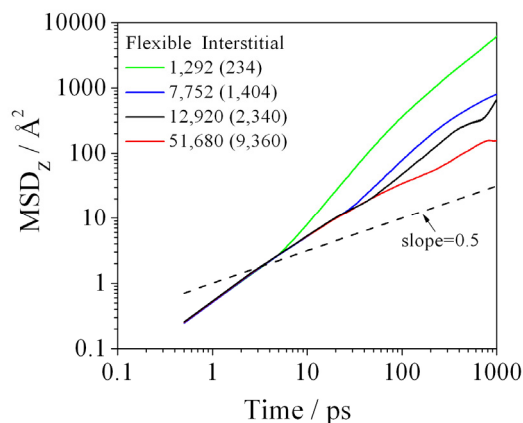
(a)



(b)



(c)



(d)

Figure 4.5: The effect of system size on the mean squared displacement as a function of the total number of argon atoms at $P/P_o = 1.2 \times 10^{-2}$. In (a) and (b) the MSD for argon atoms in the total bundle is compared for the rigid and flexible cases, respectively. In (c) and (d) the MSD for argon atoms in the interstitial sites are compared for the rigid and flexible cases, respectively. The numbers listed on the graphs indicate the total number of argon atoms in the simulation and those in the interstitial sites are in parenthesis. The dashed line illustrates the nominal slope expected for Fickian diffusion in (a) and (b) and for single-file diffusion in (c) and (d) with slopes of 1 and $1/2$, respectively.

system size do not produce large changes in the results. However, for the atoms diffusing in the interstitial sites, a total system size of 51,680 argon atoms (9,360 interstitial atoms and 42,320 inner channel atoms) may not be large enough. As shown in Fig. 4.2(d), the MSDs for the rigid and flexible cases deviate. The single-file size correlations increase with increasing density, and we believe we still have not reached a large enough system size at $P/P_o = 1.2 \times 10^{-2}$ for the interstitial sites. However, as we are attempting to compare rigid and flexible SWCNT bundles at the same system size, we have not gone to larger system sizes. A system of 51,680 argon atoms at $P/P_o = 1.2 \times 10^{-2}$ requires a SWCNT bundle with 416,000 carbon atoms. The required system sizes for higher relative pressures is also the reason we have not extended the study to pressures larger than $P/P_o = 1.2 \times 10^{-2}$.

To further illustrate the errors that can occur with using inadequate system sizes, we compare two of the smaller system sizes for $P/P_o = 6.1 \times 10^{-5}$ and $P/P_o = 1.2 \times 10^{-2}$ for the rigid and flexible SWCNT bundle simulations in Fig. 4.6. In Fig. 4.6(a) at $P/P_o = 6.1 \times 10^{-5}$ for a system size of 1,158 total argon atoms (1,080 argon atoms in the interstitial sites and 78 in the nanotube channels) we observe deviations in the MSDs for the total bundle, nanotube channel and interstitial diffusing argon atoms. The MSD for the rigid SWCNT bundles is larger than for the flexible SWCNT bundle in all cases. In Fig. 4.6(b) at $P/P_o = 1.2 \times 10^{-2}$ there is very little deviation of the MSD for the argon atoms in the nanotube channels and total bundle, but the interstitial MSDs show significant deviations at longer times and the incorrect diffusion mechanism due to the size correlation effects.

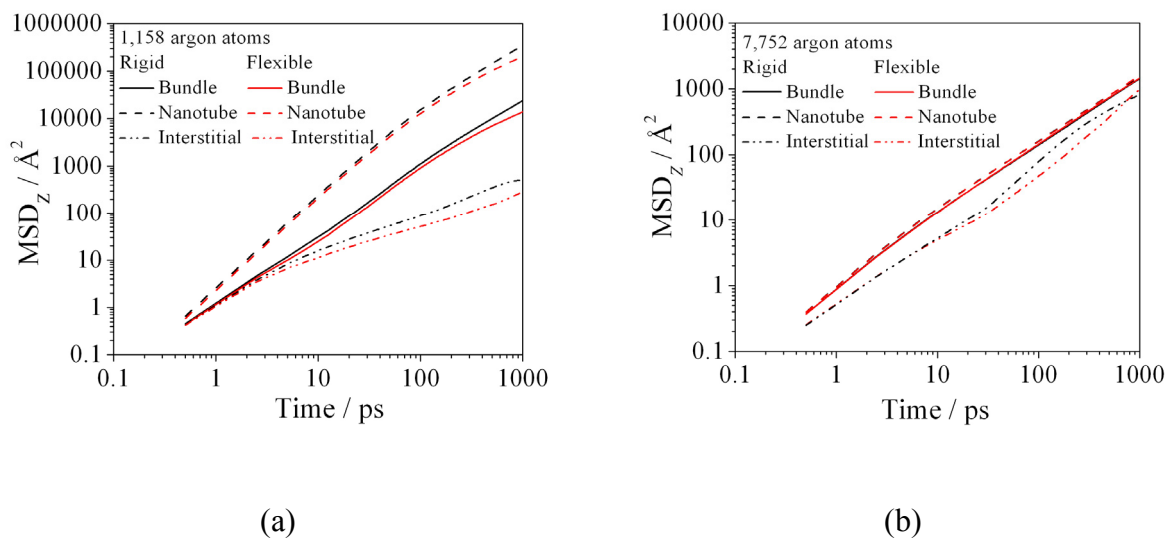


Figure 4.6: Mean squared displacement of argon along the axial direction of a (25,0) rigid (black) and flexible (red) CNT bundles in the nanotube channels (dashed), interstitial sites (dashed-dot), and total bundle (line) at 120 K and (a) $P/P_o = 6.1 \times 10^{-5}$ for a system size of 1,158 total argon atoms (1,080 interstitial and 78 nanotube channel atoms) and (b) $P/P_o = 1.2 \times 10^{-2}$ for a system size of 7,752 total argon atoms (1,404 interstitial and 6,348 nanotube channel atoms).

Inadequate system sizes also result in a center of mass drift of the fluid in the axial direction, which apart from the size correlation effect²⁷ for the single-file diffusing atoms are the major reason for deviations in the mean-squared displacements in Fig. 4.5 and Fig. 4.6. Although it has been suggested that these drifts can be subtracted off⁷¹ during the calculation of the mean-squared displacement, we found that it is not always accurate in reproducing the mean-squared displacement of the largest system size. Thus, the finite size effects cannot always be corrected for by simply subtracting the center of mass during the calculation of the mean-squared displacement, especially for atoms diffusing in single-file. All of the mean-squared displacements shown here do not have the center of mass drift subtracted.

4.4 Conclusion

Single-wall carbon nanotube bundles provide an example of a pore structure with a bimodal pore size distribution. They are composed of two different sized pores with channels inside the carbon nanotubes and smaller pores forming in interstices between the carbon nanotubes. At low pressure argon first adsorbs in the smaller interstitial sites, followed by an initial monolayer coverage of the inner nanotube walls and finally pore filling at higher pressure. For argon the inner nanotube channels give rise to Fickian diffusion with a diffusion mechanism characterized by a linear dependence of the mean squared displacement with time. The interstitial sites give rise to single-file diffusion of argon characterized by a square root time dependence of the mean squared displacement. Significant size effects exist for these quasi-one dimensional systems, and only systems that are large enough (tens of thousands and in some cases hundreds of thousands of argon atoms) yield the true diffusion mechanisms in microcanonical molecular dynamics simulations. Large size effects are observed for diffusion in the SWCNT bundle interstices where single-file diffusion occurs. Furthermore, when the size effect is taken into account, the flexibility of the SWCNT walls appears to have a small if not negligible effect on the diffusion mechanism and rates for argon, even at the lowest pressures studied. These results provide new insights into diffusion mechanisms which can occur in multi-modal porous carbon materials and speak to the difficulty of modeling diffusion in these materials.

APPENDIX

APPENDIX 4A

Correlation Effects and Center of Mass Drifts for Argon Diffusing in Isolated Single-Walled Carbon Nanotubes

In Fig. 4A.1 the size correlation effect, as previously observed by Hahn and Kärger²⁷ is shown for different system sizes of argon adsorbed in a (6,6) isolated single-walled carbon nanotube. The differences between the results in Fig. 4A.1 and the results in Chapter 1 are that these simulations have been performed without the aid of a stochastic thermostat. These simulations are molecular dynamics simulations in the microcanonical ensemble (N, V, E) which should yield the exact dynamics of the simulation. They are prepared by a 1 ns equilibration in the canonical ensemble (N, V, T) at 120 K using a Nosé-Hoover thermostat with a 0.001 ps damping coefficient, followed by a 10 ns production run using a 1 fs timestep. Prior to the start of the equilibration period using the thermostat, the linear and angular momentum of the argon atoms are zeroed. After the equilibration, the linear and angular momentum were again zeroed, and the microcanonical production began. In the microcanonical ensemble, the smallest system sizes (50 argon atoms) produced temperature fluctuations that were ± 20 K, while the largest system sizes produced temperature fluctuations that were ± 3 K, which were actually better than the thermostated fluctuations.

As a check to make sure that a 1 fs timestep was small enough, the total energy was compared for the smallest and largest system sizes with 50 and 50,000 argon atoms,

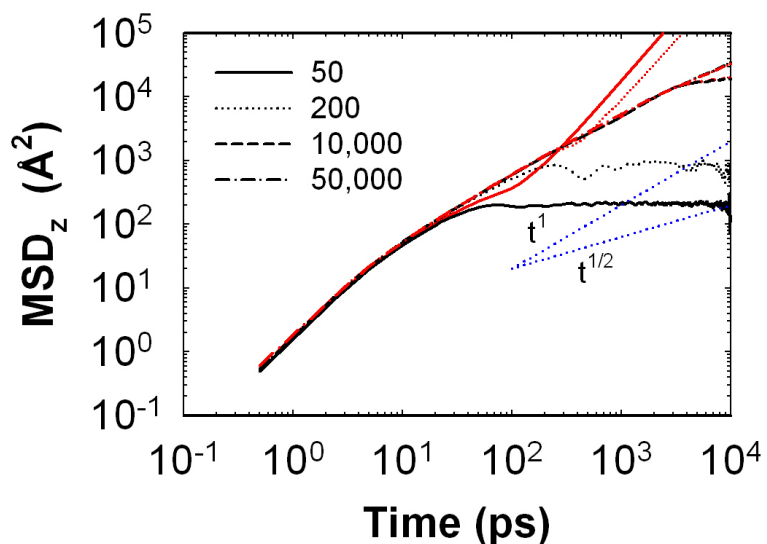


Figure 4A.1: Size correlation and center of mass drift effects for argon diffusing in infinitely long, rigid, (6,6) single-walled carbon nanotubes at 120 K and 3.66×10^{-7} bar. The number in the legend indicates the number of argon atoms diffusing inside the carbon nanotube. Red lines indicate a normal MSD calculation, while black lines indicate a MSD calculation which has had the center of mass subtracted during calculation. Dotted blue lines indicate the nominal slopes expected for single-file ($t^{1/2}$) and Fickian diffusion (t^1).

respectively. The total energy fluctuated less than 0.003 % for the 50 argon atom system. For the largest system examined utilizing 50,000 argon atoms, the energy fluctuated less than 0.0002 %. To obtain larger system sizes, the configuration with 50 argon atoms was replicated a number of times in the axial direction, using the periodic boundary.

In Fig. 4A1 several lines are shown. Those in red represent a normal calculation of the mean-squared displacement (MSD). Those in black represent the same calculation, but with the center of mass (COM) subtracted during each measurement. This can be performed

using Eq. (4A.1):

$$MSD_{\text{COM}} = \left\langle \sum_{i=1}^N (\Delta z_i(t) - \Delta z_i(0))^2 \right\rangle \quad (4A.1)$$

where

$$\Delta z_i(t) = z_i(t) - \frac{\sum_{i=1}^N z_i(t) MW_i}{\sum_{i=1}^N MW_i} = z_i(t) - z_i^{\text{COM}}(t) \quad (4A.2)$$

Fig. 4A1 also shows dotted lines which represent the nominal slope for single-file diffusion expected (1/2) and for Fickian diffusion (1) on the log-log scale. For 50 argon atoms without the center of mass subtracted (red solid line in Fig. 4.A1) in the (6,6) carbon nanotube, the diffusion shows a ballistic region at small times (sub-picosecond), followed by a transition to a MSD with a slope which also exhibits ballistic behavior at long times (a slope of 2 on the log-log scale). A similar observation is made for the system with 200 particles. After the center of mass is subtracted using Eq. (4A.1), the 50 particle system (solid black line in Fig. 4.A1) exhibits the normal ballistic behavior at short times, followed by a finite value of the MSD at long times with small oscillations. The same is observed for the 200 particle system. Much larger system sizes are needed to remove both 1) the size correlation effect and 2) the center of mass drift. For system sizes of 10,000 and 50,000 argon atoms, both of these effects nearly vanish, and both the red line (MSD without the center of mass subtracted) and the black line (MSD with the center of mass subtracted) fall on top of each other. A size correlation effect is apparent for the data at very long times for

the 10,000 atom systems as both the MSD with and without the center of mass subtracted approach a finite value near 10 ns (10^4 ps). However, below 1 ns (10^3 ps) both the 10,000 and 50,000 systems appear to be of adequate size, as both the center of mass drift and the size correlation effect are negated.

To illustrate the influence of the center of mass drift on the mean-squared displacement, the center of mass drift is shown in Fig. 4A.2 for 50, 200, 10,000, and 50,000 argon atoms. For system sizes of 50 and 200 argon atoms, there is a dramatic drift of the center of mass, despite the fact that both the linear (directly related to the velocity center of mass) and angular momentum were zeroed prior to the start of the microcanonical molecular dynamics simulations in all cases. The drift is smaller as the system size increases. For 10,000 and 50,000 argon atoms the drift is much smaller, with appreciable drift only occurring at long times where the MSD is orders of magnitude larger.

Once the center of mass drift effects as well as the size correlations effects are diminished using adequate system sizes, the effect of pore flexibility becomes negligible. Keil and coworkers^{48, 54, 55} using system sizes less than 100, showed that at low pressures, nanotube flexibility had an influence on the diffusion of fluids within pores. However, as we show in Fig. 4A.3, when adequate system sizes are used, this does not seem to be the case for argon. This is due to the smoothness of the carbon nanotubes³⁴. Bhatia and coworkers³⁴ as described in Chapter 1, showed that the diffusive collisions of hydrogen were negligible.

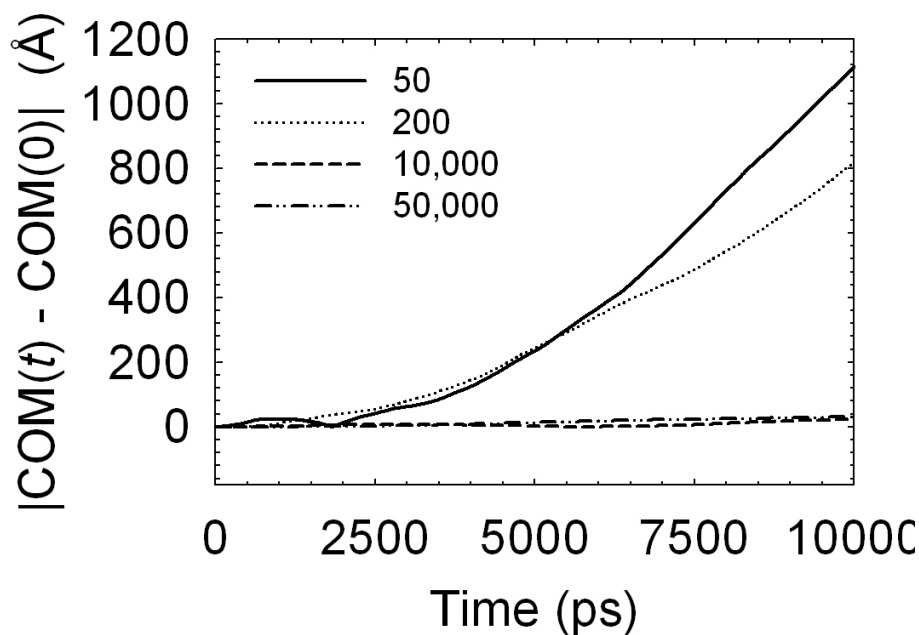


Figure 4A.2: The center of mass (COM) drift of argon atoms during microcanonical molecular dynamics simulations for argon in a (6,6) isolated, single-walled carbon nanotube at 120 K and 3.66×10^{-7} bar. System sizes using only 50 or 200 argon atoms show significant center of mass drift, while those with 10,000 and 50,000 argon atoms show smaller drift at longer times.

Argon which is larger in molecular diameter than hydrogen should exhibit less diffusive collisions than hydrogen. The alkane molecules that Keil and coworkers examined should exhibit even less. Evidence of this can be found in the work of Cruz and Müller³³ who studied the diffusion of alkanes in single-file in carbon nanotubes. They found MSDs which did not exhibit the expected anomalous sub-diffusive behavior for single-file diffusion. They used a deterministic Nosé-Hoover thermostat. Striolo³¹, who also used a deterministic

Nosé-Hoover thermostat, found that water diffusing in single-file in carbon nanotubes exhibits long time linear or ballistic behavior.

This is further exhibited by the fact that argon, as shown in Fig. 4A.3(a) for both the flexible and rigid cases for single-file diffusion, exhibits a linear dependence of the MSD with time, rather than the expected square root of time dependence. When the system is thermostated with a stochastic thermostat, as shown in Fig 4A.3(a), argon exhibits the expected square root of time dependence for single-file diffusion². Thus, the stochastic thermostat is mimicking the surface corrugation needed to produce diffusive collisions of argon atoms with the nanotube wall. However, this effect is unrealistic, as the carbon nanotube in fact has very little corrugation, as indicated by the microcanonical results.

In Fig. 4A.3(b) the case of argon diffusing by a Fickian mechanism in a (10,10) carbon nanotube is shown. The influence of flexibility is negligible as it was for the (6,6) case. While the Langevin thermostated case for the (10,10) carbon nanotube produces the same diffusion mechanism as the microcanonical simulations, the diffusional rate is much slower. The Langevin thermostat mimicks too much diffusive reflection of argon atoms with the carbon nanotube wall and produces a diffusion coefficient that is too small.

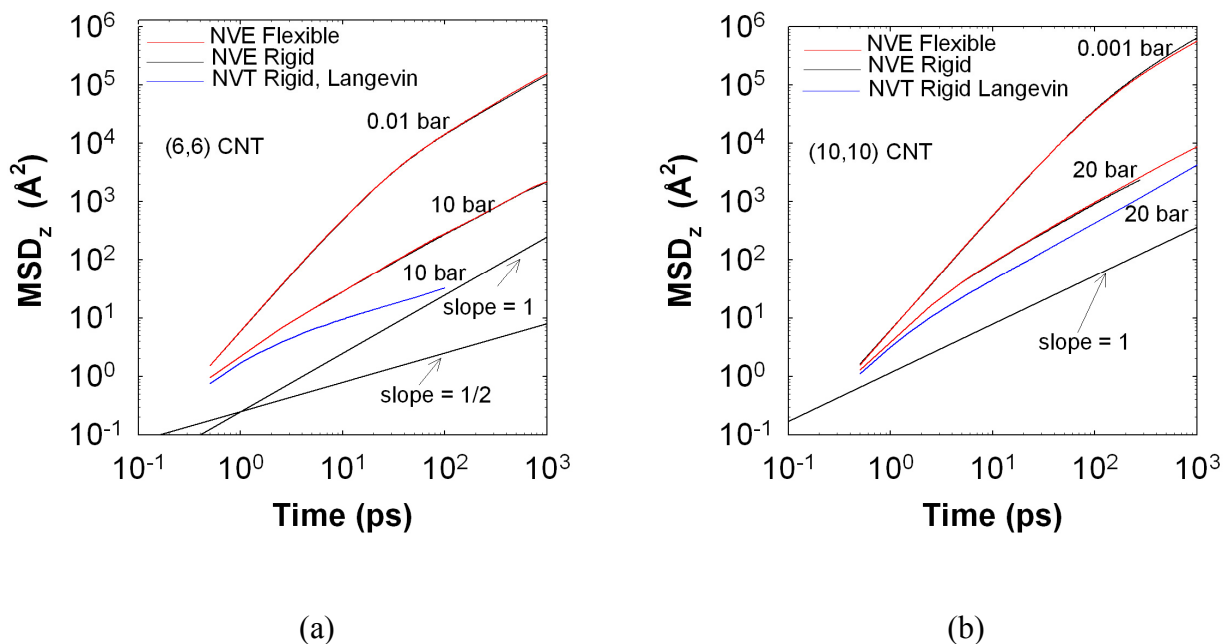


Figure 4A.3: (a) Argon diffusing in single-file in a (6,6) CNT at 298 K. At 0.01 bar there are 1,536 argon atoms in the microcanonical simulations. At 10 bar, there are 27,904 argon atoms in the microcanonical simulations. (b) Argon diffusing in three-dimensions in a (10,10) CNT at 298 K. At 0.001 bar there are 500 argon atoms in the microcanonical simulations. At 20 bar there are 5,760 argon atoms in the microcanonical simulations. In both figures red lines indicate microcanonical simulations with a flexible CNT wall, black lines indicate microcanonical simulations with a rigid CNT wall. The blue line indicates a canonical simulation using a stochastic Langevin thermostat. In (a) there were 109 argon atoms in the Langevin simulation at 10 bar and in (b) there were 288 argon atoms in the Langevin simulation.

CHAPTER 5

Anomalous Diffusion in Ordered and Disordered Microporous Carbons

5.1 Introductionⁱ

In Chapters 2-4 single-file diffusion of argon was investigated in carbon nanotubes and carbon nanotube bundles. In this chapter, diffusion is studied in models of a disordered activated carbon and an ordered model of a carbon replica of a zeolite. Both materials exhibit a maximum in their diffusion coefficients as well as *anomalous* (sub-diffusive) behavior in their mean-squared displacements at short times at some relative pressures. In the activated carbon, the anomalous diffusion occurs at low relative pressures, due to the trapping of argon atoms in small pores. In the carbon replica of zeolite, the anomalous diffusion occurs at high relative pressures, due to competitive diffusion of atoms traveling through windows and constrictions which interconnect the pores. All diffusion eventually tends toward the Fickian limit at longer times.

Microporous carbons have found recent interest in many areas including chemistry, chemical engineering and materials science, due to their potential for use in separation and

ⁱ Material from this chapter has been published in J.D. Moore, J.C. Palmer, Y.C. Liu, T.J. Roussel, J.K. Brennan, and K.E. Gubbins, "Adsorption and Diffusion of Argon Confined in Ordered and Disordered Microporous Carbons", Applied Surface Science, 256, 5131-5136 (2010). Reprinted with permission from Elsevier, Copyright (2010).

storage of gases. They exist in both ordered (*e.g.*, carbon nanotubes, slit pores consisting of graphene layers, and carbon replicas of zeolites) and disordered (*e.g.*, charcoal, carbon soot, and activated carbon) forms.

Activated carbons are amorphous materials that have found widespread use in industry due to their low production cost, high adsorption capacity and predominately microporous (pores < 2 nm) features⁷²⁻⁷⁴. Calgon Co.'s bituminous coal-based carbon (BPL) is among the most widely studied activated carbons and has been used extensively in environmental applications as an adsorbent for the removal of toxic and odorous industrial chemicals⁷⁵. Palmer *et al.*⁷⁶ have recently developed a morphologically realistic model of BPL, using the Hybrid Reverse Monte Carlo method^{77,78}, that successfully predicts the adsorptive properties of the real material.

A second class of materials which has generated recent interest are carbon templates of mesoporous silica materials such as MCM-41, SBA-15 or various microporous zeolites⁷⁹⁻⁸¹. This type of material is inherently highly ordered. A carbon replica of the zeolite Faujasite (C-FAU) has shown potential application in the areas of hydrogen storage and in the development of hydrogen fuel cells^{82, 83}. Using a mimetic Grand Canonical Monte Carlo templating process, Roussel *et al.*⁸³ have modeled C-FAU and when compared with experiment found reasonable agreement for its structural and adsorptive properties.

Simulation studies of the diffusion of fluids in microporous carbons are not very numerous, with the exception of studies of diffusion in cylindrical pores using Lennard-Jones (LJ) potentials with smooth model walls⁸⁴, hard spheres with smooth model walls^{19, 22-24}, and LJ particles and alkanes in atomically detailed carbon nanotubes^{48, 54, 70, 85}. Gubbins and co-workers studied the diffusion of LJ fluids in several saccharose derived carbons^{36, 37, 86, 87} generated by the Hybrid Reverse Monte Carlo method and found a maximum in the diffusion coefficient as a function of loading. Experimentally, maxima in the diffusion coefficient are well known for molecular fluids diffusing in zeolites⁸⁸ and have been observed for water diffusing in activated carbon³⁹.

Diffusion in porous materials can occur by three types of mechanism. *Ballistic* motion occurs for very short times, before molecules have had a chance to collide, and the mean squared displacement (MSD) of molecules is proportional to the time². For longer times, the motion is either *completely diffusive* (Fickian) or *sub-diffusive*. For sufficiently large pores, the molecules will diffuse in three-dimensions as they would in a bulk fluid, and the MSD is proportional to time. However, in smaller pores where confinement effects dominate, the diffusion is sub-diffusive. The most well known form is that of anomalous, or single-file, self-diffusion⁹, which can be shown to have a MSD proportional to time^{1/2} if there is no passing of particles in the pore². This has been studied extensively in model cylindrical pores by Hahn and Kärger^{84, 89} and Mon and Percus^{18-20, 22, 24, 25}. Depending on the degree

of confinement and the frequency of particles passing in the material, the MSD dependence with time can be between $1/2$ and 1 ⁸⁹.

In this work, using microcanonical molecular dynamics simulations, we compare the self-diffusion of argon confined in the Palmer *et al.*⁷⁶ activated carbon model of BPL and in the Roussel *et al.*⁸³ model of C-FAU and demonstrate that the microporous features of the materials lead to sub-diffusive diffusional behavior at short times. Anomalous regions appear in the MSDs depending on the pore filling of the materials, but eventually molecules in these regions escape into larger pores and tend to completely-diffusive Fickian behavior at longer times. The anomalous regions contribute to the maximum in the diffusion coefficient previously observed by others.

5.2 Computational Methods

5.2.1 Monte Carlo Simulations

Grand Canonical Monte Carlo (GCMC) simulations were used to calculate adsorption isotherms for argon at 77 K and 120 K for the two rigid carbon structures, BPL and C-FAU. In the context of this work, the GCMC method simulates the chemical equilibrium reached between a fictitious gas reservoir containing bulk argon and the adsorbed argon phase in the carbon structures. Chemical equilibrium is reached when the chemical potential of the two

phases are equal. The bulk argon phase was treated as an ideal gas under the state conditions examined in this study, which allowed for the chemical potential and pressure of the bulk phase to be related by using the ideal gas equation of state. The difference between the absolute amount adsorbed as calculated using GCMC and the excess amount adsorbed was negligible under the examined state conditions. Thus, no additional corrections were applied to the simulated isotherms.

Both argon and carbon were modeled as Lennard-Jones atoms with $\epsilon_{Ar-Ar} / k_B = 124.07 \text{ K}$ and $\sigma_{Ar-Ar} = 0.342 \text{ nm}$, and $\sigma_{C-C} = 0.340 \text{ nm}$ and $\epsilon_{C-C} / k_B = 28.00 \text{ K}$ for argon and carbon, respectively. The parameters for the argon-carbon interaction parameters were estimated using the Lorentz-Berthelot combining rules, $\sigma_{ij} = (\sigma_{ii} + \sigma_{jj}) / 2$ and $\epsilon_{ij} = \sqrt{\epsilon_{ii}\epsilon_{jj}}$, to yield $\sigma_{Ar-C} = 0.341 \text{ nm}$ and $\epsilon_{Ar-C} / k_B = 58.94 \text{ K}$. Periodic boundary conditions were applied to the unit cells in all three directions and the pair-wise interactions were evaluated using the minimum image convention. The cubic unit cell lengths were 30.0 Å for BPL and 49.7 Å for C-FAU. Prior to the start of the simulations, the argon-carbon interactions were calculated at 15.625×10^6 evenly-spaced grid points that spatially discretized the unit cell containing the carbon structure. These values were then stored and used during the simulations to calculate the argon-carbon interactions using a linear interpolation scheme.

For each state point, the system was equilibrated using a minimum of 2.5×10^8 Monte Carlo trials, followed by an additional 2.5×10^8 trials over which statistics were collected. Each Monte Carlo trial consisted of an attempted translation, insertion, or deletion of an argon molecule. The final argon configurations were used as the initial configurations for the simulations at subsequent state points in the isotherms.

5.2.2 Molecular Dynamics Simulations

The dynamical properties of the adsorbed argon were examined using molecular dynamics (MD) simulations with the LAMMPS (Large-scale Atomic/Molecular Massively Parallel Simulator) simulation package⁶¹. At each state point along the isotherms, the equilibrated configurations obtained from the GCMC simulations were replicated using the periodic boundary conditions of the unit cells to form supercells containing a minimum of 1,000 argon atoms. This was done to ensure that adequate statistics could be gathered even under low-loading conditions, where a single unit cell may only contain a small number of argon atoms. The supercell configurations were then equilibrated for 1 ns in the canonical ensemble (NVT) using the Nosé-Hoover thermostat to control the temperature and a 1 fs timestep to integrate the equations of motion. Following equilibration, runs were performed on each system in the microcanonical ensemble (NVE) with a 1 fs timestep. Because of the large system size ($> 1,000$ fluid atoms), the temperature fluctuated within ± 3 K in all of the simulations, even in the microcanonical simulations. The resulting microcanonical MD

trajectories were used to measure the mean squared displacement (MSD) of the argon atoms. In all of the MD simulations, the potential energy and force calculations were performed using the same Lennard-Jones models for argon and carbon as in the GCMC simulations.

5.3 Results and Discussion

5.3.1 Adsorption

The adsorption isotherms for argon were measured in BPL and C-FAU at 77 K and 120 K using GCMC simulations, and are shown in Fig. 5.1. To compare the structures at different temperatures, we have normalized the amount adsorbed, Γ , by the amount adsorbed at $P_o(T)$ (the bulk vapor pressure of argon), Γ_o . Thus for BPL, these amounts were calculated using $\Gamma_o = 15.2$ mmol/g at 77 K and $\Gamma_o = 13.6$ mmol/g at 120 K, while those for C-FAU were calculated using $\Gamma_o = 28.7$ mmol/g at 77 K and $\Gamma_o = 26.5$ mmol/g at 120 K. The pressure on the x-axis in Fig. 5.1 is normalized by the bulk vapor pressure of argon, which was calculated using the LJ equation of state⁶³ with the LJ parameters of argon used in this study. These were measured as 0.19 atm at 77 K and 8.1 atm at 120 K. For both structures, argon exhibits a Type I isotherm according to the IUPAC classification, with no observable hysteresis upon desorption. For the sake of clarity, we have omitted the desorption results and have shown the isotherms with the pressure on a log-scale in order to illuminate the pore filling-regions of the isotherms.

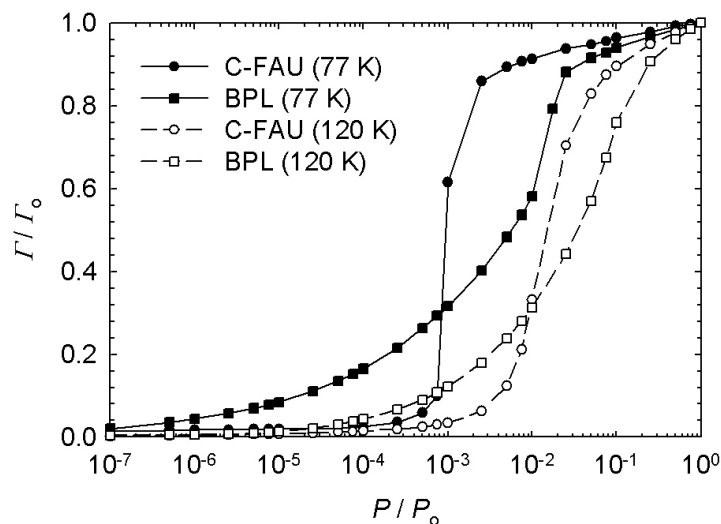


Figure 5.1: Adsorption isotherms for argon at 77 K (closed) and 120 K (open) in C-FAU (circles) and BPL (squares).

At both 77 K and 120 K, argon begins to appreciably fill C-FAU at a larger relative pressure than BPL but also fills the structure over a shorter pressure range. This behavior can be explained by comparing the pore size distributions (PSDs) of BPL and C-FAU, shown in Fig. 5.2. The PSDs were measured geometrically using the method of Gelb and Gubbins⁹⁰ with a probe particle diameter the same as the LJ model of argon used in this study. BPL has a broader PSD with an average pore size of 8.3 Å, while C-FAU has a narrower PSD with an average pore size of 10.9 Å. The higher fraction of smaller pores in BPL enhances its ability to adsorb argon at lower pressures, due to the increased degree of confinement felt by the argon molecules in the smaller pores of the solid matrix, while the larger pores in C-

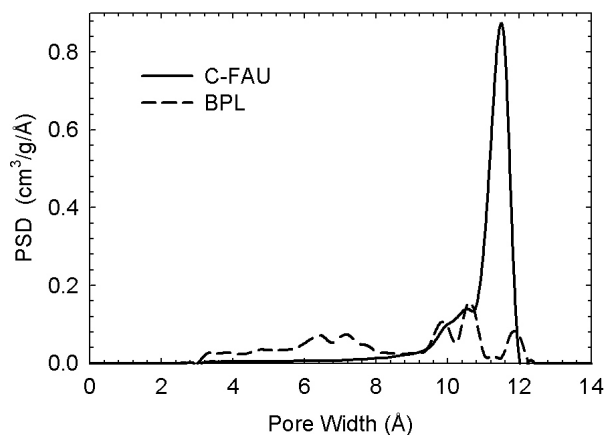


Figure 5.2: Pore size distributions for argon in C-FAU and BPL.

FAU shift the onset of pore filling to larger relative pressures at the same temperature. This is further illustrated by considering the simulation snapshots shown in Fig. 5.3. At 120 K for BPL, argon atoms are first adsorbed appreciably in smaller pores at low relative pressures (*e.g.*, $P/P_o \sim 10^{-5}$). At a relative pressure of $P/P_o \sim 10^{-3}$ the smaller pores have almost completely filled with adsorbate, while larger pores have already begun to fill. In the isotherm in Fig. 5.1, this corresponds to the start of the pore filling region previously mentioned. As the relative pressure is increased, the larger pores continue to fill until saturation is reached. Conversely for the C-FAU model, because of its narrower PSD and larger accessible pores, an appreciable adsorption does occur at $P/P_o \sim 10^{-3}$ but then the larger pores are quickly filled and are almost completely filled at $P/P_o \sim 0.10$. Similar results occur at 77 K, except that the pressure ranges are shifted to the left, as more adsorption of argon occurs at lower relative pressure for a lower temperature.

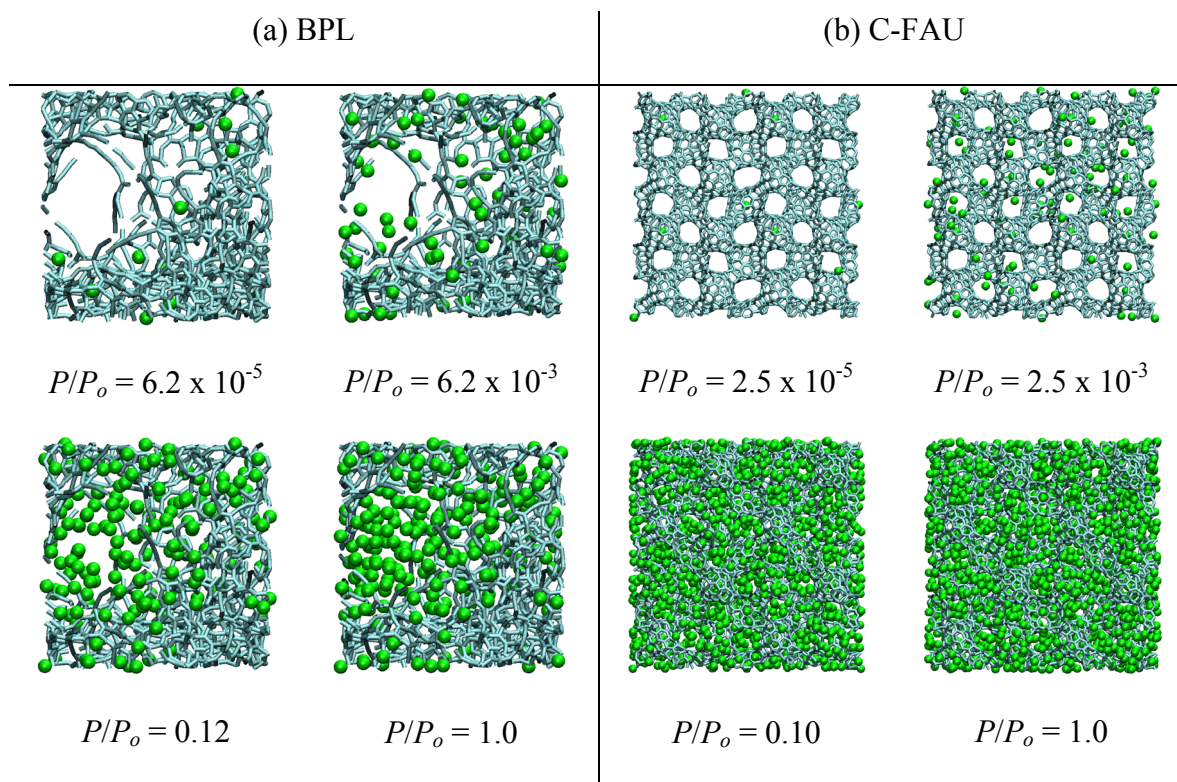
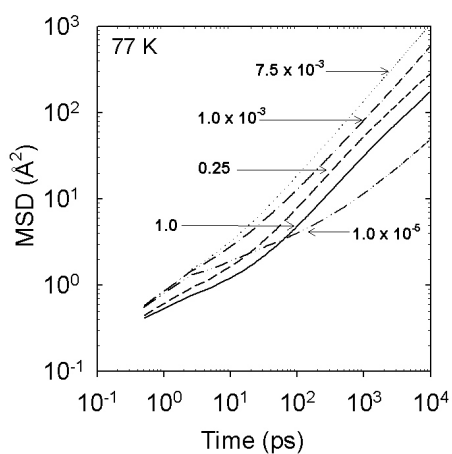


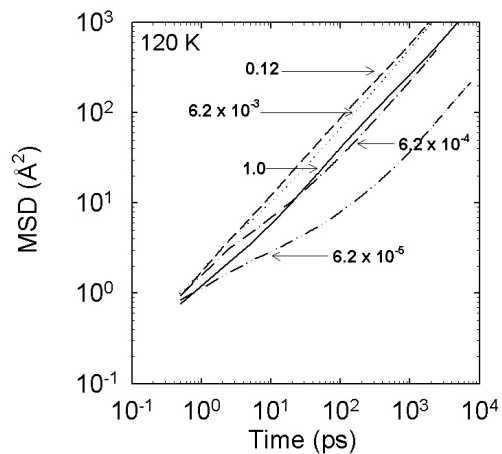
Figure 5.3: Simulation snapshots of argon adsorbed in BPL and C-FAU at 120 K and various relative pressures. Snapshots at 77 K are similar for comparable fractional fillings along the isotherm.

5.3.2 Diffusion

The mean squared displacements (MSDs) measured from the microcanonical (NVE) MD simulations for BPL and C-FAU are shown in Figs. 5.4 and 5.5, respectively. In Fig. 5.4(a) for BPL at 77 K, all of the MSDs exhibit a small slope for short times, changing to a

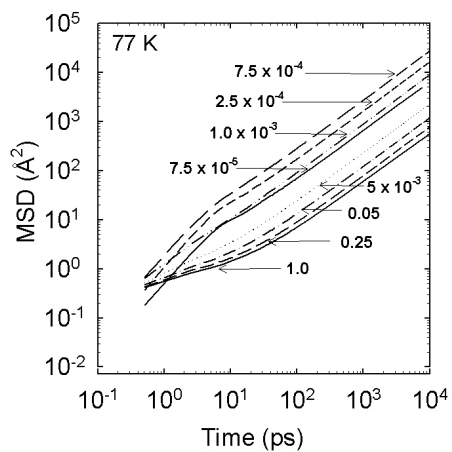


(a)

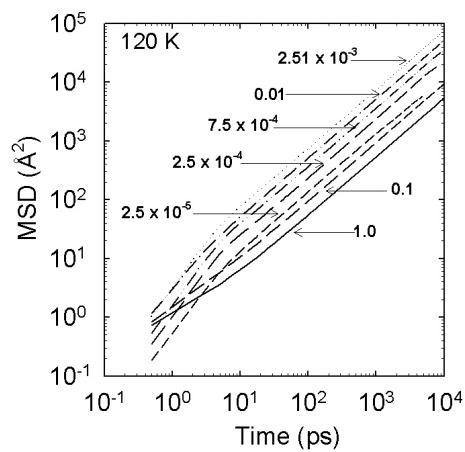


(b)

Figure 5.4: Mean squared displacements for argon diffusing in BPL activated carbon at various relative pressures, $P/P_o(T)$, at (a) 77 K and (b) 120 K.



(a)



(b)

Figure 5.5: Mean squared displacements for argon diffusing in C-FAU, the carbon replica of Faujasite, at various relative pressures, $P/P_o(T)$, at (a) 77 K and (b) 120 K.

steeper slope as time increases. The effect is most evident at the lowest pressure ($P/P_0 = 1.0 \times 10^{-5}$), where the increase in the slope does not begin until approximately 1 ns (1,000 ps). On the log-log scale, the slope at shorter times is closer to 1/2, which is analogous to the slope seen for anomalous single-file diffusion in cylindrical pores⁹ (e.g., carbon nanotubes and carbon nanotube bundles⁵¹). The slopes for higher pressures are greater than 1/2, but less than 1, which indicates a sub-diffusive behavior (*i.e.*, not following the normal Fick's Law of diffusion). At the longest times, all of the slopes of the MSDs approach 1, indicating eventual diffusive (Fickian) behavior. In Fig. 5.4(b) for BPL at 120 K, similar effects are seen, except that the anomalous initial mode of diffusion is not as evident except for reduced pressures less than 10^{-3} . Above relative pressures of 10^{-3} , the MSDs at 120 K do not exhibit strong effects due to anomalous diffusion.

C-FAU also exhibits anomalous regions in its MSDs at 77 K and 120 K. These are shown in Fig. 5.5(a) for 77 K and Fig. 5.5(b) for 120 K. At 77 K, anomalous regions are observed in the MSDs for pressures above $P/P_0 \sim 10^{-3}$. This is in contrast to the behavior seen in the BPL model, where the anomalous regions were present below $P/P_0 \sim 10^{-3}$. At 120 K, anomalous regions are observed for short times only above $P/P_0 \sim 0.1$. For the C-FAU model, below $P/P_0 \sim 10^{-3}$ at 77 K and below $P/P_0 \sim 0.1$ at 120 K, the diffusion follows the usual path, with an initial ballistic (free-flight) motion below 10 ps observed with a $time^2$ dependence of the MSD, followed by Fickian diffusion for times greater than ~ 10 ps and a $time^1$ dependence of the MSD.

We note that there is an absence of the ballistic region observed in BPL and C-FAU when an anomalous region is observed at short times. In such cases, the short time behavior is completely dominated by the anomalous motion. In the C-FAU model, at low pressures when there is an absence of the appearance of the anomalous region, the ballistic region is observed at short times. This suggests several effects. In the BPL model, the anomalous region is caused by atoms initially trapped in small, attractive pores with their movement slowed until atoms eventually escape the small pores and are able to diffuse into the larger pores, which is consistent with the eventual long-time mode of diffusion being Fickian. Even at small times (typically $< 10 \text{ ps}^{51}$), where ballistic (free-flight) motion is expected to occur, the atoms are already colliding with the wall and therefore do not exhibit a ballistic motion on this time scale. Note that we did not sample the mean squared displacement below 0.5 ps, and a ballistic motion possibly would be observed at this very short time scale. At higher pressure ($\sim P/P_o > 10^{-3}$), the atoms are also initially trapped within the small pores, but the faster Fickian diffusion in the larger pores dominates the overall molecular motion and the anomalous regions are not as apparent. However, because of the short time collisions with the wall, atoms trapped within small pores do not exhibit ballistic motion on the time scales shown in Fig. 5.4. In fact at short times ($< 1 \text{ ps}$) the MSDs observed for BPL at 77 K in Fig. 5.4(a) are sub-diffusive.

For C-FAU, anomalous diffusion is observed only at higher relative pressure while not at lower relative pressure. This suggests that the anomalous regions in the MSDs for C-FAU

are not caused by the trapping of atoms in small pores but by the traffic caused by particles moving through the windows and constrictions interconnecting the pores. As is evident from the PSD for C-FAU in Fig. 5.2, C-FAU does have pores of different diameters caused by these windows and constrictions, and these are much larger than the smallest accessible pores for argon in BPL. Therefore, trapping within small pores does not occur in C-FAU. The trapping of atoms in small pores of the BPL model as well as the traffic of atoms traveling between the windows and constrictions interconnecting the pores in the C-FAU model was confirmed from atomic configuration movies of the molecular dynamics simulations.

Typically, the MSD should decrease with increasing pressure since the higher density slows the diffusion of all the other atoms in the material. However, in both BPL and C-FAU, there is a ‘cross-over’ of the diffusion which appears to occur at pressures corresponding to the onset of pore-filling observed in the isotherms in Fig. 5.1. For BPL at 77 K, this pressure is close to $P/P_o = 7.5 \times 10^{-3}$. For relative pressures less than this, diffusion increases with increased relative pressure, as more particles are being adsorbed into larger pores where they can diffuse faster by a Fickian mechanism. For relative pressures greater than $P/P_o = 7.5 \times 10^{-3}$, diffusion is slowed for the usual reason that the increased density slows the overall diffusion of all the other atoms. For BPL at 120 K, this ‘cross-over’ pressure is closer to $P/P_o \sim 10^{-2}$. Despite the anomalous region occurring at higher pressure rather than lower pressure in C-FAU, a ‘cross-over’ occurs at $P/P_o \sim 7.5 \times 10^{-4}$ at 77 K and $P/P_o \sim 2.5 \times 10^{-3}$ at 120 K. In Fig. 5.6, these ‘cross-overs’ cause a maximum to occur in the self-diffusion

coefficient, which is located at relative pressures corresponding to the pore-filling region of the isotherm.

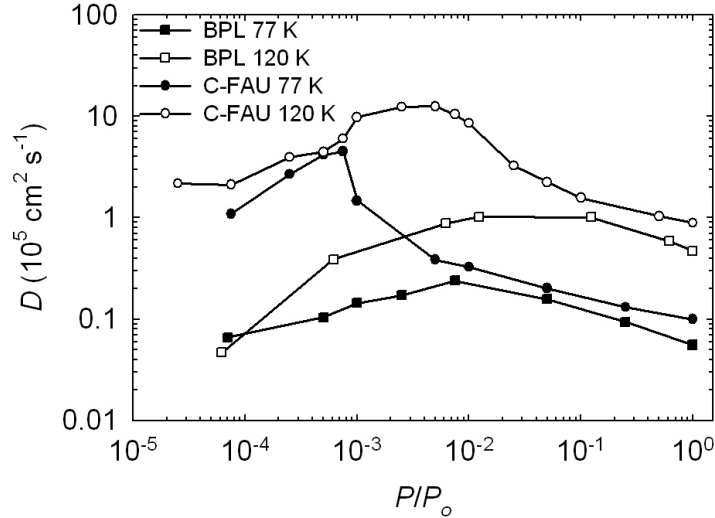


Figure 5.6: Self-diffusion coefficients for argon in BPL (squares) and C-FAU (circles) at 77 K (open) and 120 K (closed).

5.4 Conclusions

The diffusion of argon in the BPL and C-FAU models exhibits a maximum in the diffusion coefficient at a particular pressure at both 77 K and 120 K. In the BPL model, this maximum is the result of atoms initially diffusing in small pores. As the pore is filled, the diffusion increases initially as more molecules begin to diffuse in larger pores. As the density of atoms within the larger pores is increased further, the diffusion begins to slow.

Because of the trapping of atoms within small pores, at low loading the mean-squared displacement exhibits sub-diffusive, anomalous behavior. The anomalous regions are enhanced at lower temperature, with more sub-diffusive behavior occurring at higher relative pressures. In C-FAU, the maximum in the diffusion coefficient arises for similar reasons. At intermediate loading more atoms diffuse in larger pores, initially increasing the diffusion coefficient. As the pressure is further increased the increase in density in the larger pores causes the diffusion coefficient to decrease. Because of the narrow pore size distribution for C-FAU with multiple windows and constrictions interconnecting pores, anomalous regions appear because of competitive diffusion of atoms traveling between these windows and constrictions at the highest relative pressures. This is the opposite effect to that seen in the disordered BPL, where anomalous regions appear at the lowest relative pressures. In C-FAU, the anomalous regions are also enhanced at lower temperature with more sub-diffusive behavior occurring at lower relative pressures. The eventual diffusion mechanism in both materials is always Fickian, but because the anomalous behavior can occur up to times of 1 ns or greater, one must be careful to measure the mean squared displacements at sufficiently long times. We have used microcanonical molecular dynamics simulations, which should give rise to the correct dynamics within the framework of our models.

CHAPTER 6

Conclusions and Outlook

In this work, we have shown examples of single-file and anomalous diffusion in porous carbons. Carbon nanotubes are inherently smooth³⁴. For Fickian diffusion this has the benefit that faster modes of diffusion are possible than in other more corrugated materials such as zeolites^{56, 64}. However, if one wishes to study single-file diffusion, this smoothness leads to a lack of diffusive reflection for collisions of molecules with the wall and a violation of the random walk needed to observe the slower square root of time dependence of the mean-squared displacement.

We showed, however, that surface corrugation, mimicked using a stochastic Langevin thermostat does produce the slower square root of time dependence. In experiment, carbon nanotubes possess a range of defects, including bends, junctions⁴⁷, and vacancies. Future investigation of single-file diffusion could investigate the influence that these defects have on the diffusive collisions with the wall, and what, if any, type of defects lead to slower modes of diffusion in carbon nanotubes. Single-file diffusion with the square root of time dependence was observed for carbon nanotube bundles within interstitial sites, without the aid of a stochastic thermostat, and using microcanonical simulations. This was the result of corrugation caused by argon atoms colliding with the outside walls of nanotubes in the bundle.

While a stochastic thermostat was useful to understand general physics concerning the molecular size of adsorbed molecules needed to observe the square root of time dependence of single-file diffusion, only microcanonical simulations gave accurate depictions of the true diffusion mechanism. However, we showed that these microcanonical simulations for carbon nanotubes lead to numerical anomalies concerning size correlation lengths and center of mass drift that are of particular importance for single-file diffusion. These appear to only be corrected in the limit of very large system sizes. For rigid nanotube simulations, 50,000 – 100,000 adsorbate atoms take no more than a few days to simulate on large supercomputers, but using this number of fluid atoms with flexible walls can take much longer. However, when the system size approaches the needed limit, pore flexibility appears to have a negligible effect on the self-diffusion of argon. As many other fluids, including water, have fluid-wall interaction energies (with carbon) that are similar magnitude or smaller, carbon nanotube flexibility is expected to be negligible for those fluids as well. For similar reasons, at normal temperatures (above 25 K or so), most fluids diffusing in bare carbon nanotubes should not show a chirality dependency. This was observed in Chapter 2 for argon diffusing in various chiralities of carbon nanotubes. It may be possible to observe a chirality effect by decorating the carbon nanotube walls with functional groups. This would increase the fluid-wall interaction energies, especially for polar adsorbate molecules such as water. Future investigations should examine single-file diffusion of water in carbon nanotubes, zeolites, and other one-dimensional pores to see whether collective motion is caused by these numerical anomalies or whether hydrogen bonding also plays a role.

Models of activated carbon and a carbon replica of zeolite exhibited anomalous regions in the MSDs, with the slope of the MSD approaching 1/2 at low relative pressures for activated carbon and high relative pressures in the carbon replica of zeolite. In the activated carbon this was caused by trapping of molecules within small, highly attractive pores at lower pressure. At higher pressures this anomaly seemingly disappeared as the motion of the molecules in the larger pores contributed much more to the MSD than those in the smaller pores. Diffusion of argon in the carbon replica of zeolite did not show anomalous diffusion at lower pressure because the material did not contain small pores. However, at higher pressure, anomalous diffusion existed at small times, due to competitive diffusion of argon atoms between windows and constriction which slowed diffusion. Future investigation concerning diffusion in porous materials should investigate diffusion modes within different pore sizes of the material, connecting the pore size distribution to the diffusion coefficient and diffusional mechanisms.

This study focused only on self-diffusion. Future investigation into anomalous diffusion could provide an extension to transport diffusion (the diffusion directly related to Fick's first law) in pure components and mixtures. In Chapter 3, we examined various mixtures diffusing in carbon nanotubes, and calculated their individual self-diffusivities. This provided an analysis via the mean-squared displacements and the self-diffusion coefficients and single-file mobilities. However, this study should be extended to calculate mixture diffusivities. This may involve the mutual diffusivity^{91, 92} based on an Onsager^{93, 94}

formulation and Fick's law or others including the Maxwell-Stefan formulation⁹⁵⁻⁹⁷.

Transport diffusion for pure components and mixtures⁹⁸ should also be investigated in carbon nanotube bundles, models of activated carbon, as well as carbon replicas of zeolites. Within these materials, a formulation which connects different diffusion modes occurring within different porous regions of the material would be useful.

REFERENCES

- 1 D. G. Levitt, *Phys. Rev. A*, 1973, **8**, 3050-3054.
- 2 B. U. Felderhof, *J. Chem. Phys.*, 2009, **131**, 064504.
- 3 T. E. Harris, *J. Appl. Prob.*, 1965, **2**, 323-338.
- 4 F. Spitzer, *Adv. Math.*, 1970, **5**, 246-&.
- 5 P. M. Richards, *Phys. Rev. B*, 1977, **16**, 1393-1409.
- 6 P. A. Fedders, *Phys. Rev. B*, 1978, **17**, 40-46.
- 7 S. Alexander and P. Pincus, *Phys. Rev. B*, 1978, **18**, 2011-2012.
- 8 H. van Beijeren, K. W. Kehr and R. Kutner, *Phys. Rev. B*, 1983, **28**, 5711-5723.
- 9 K. Hahn, J. Karger and V. Kukla, *Phys. Rev. Lett.*, 1996, **76**, 2762-2765.
- 10 V. Gupta, S. S. Nivarthi, A. V. McCormick and H. T. Davis, *Chem. Phys. Lett.*, 1995, **247**, 596-600.
- 11 V. Kukla, J. Kornatowski, D. Demuth, I. Gimus, H. Pfeifer, L. V. C. Rees, S. Schunk, K. K. Unger and J. Karger, *Science*, 1996, **272**, 702-704.
- 12 Q. H. Wei, C. Bechinger and P. Leiderer, *Science*, 2000, **287**, 625-627.
- 13 C. Lutz, M. Kollmann and C. Bechinger, *Phys. Rev. Lett.*, 2004, **93**, 026001.
- 14 B. H. Lin, M. Meron, B. X. Cui, S. A. Rice and H. Diamant, *Phys. Rev. Lett.*, 2005, **94**, 216001.
- 15 A. Das, S. Jayanthi, H. S. M. V. Deepak, K. V. Ramanathan, A. Kumar, C. Dasgupta and A. K. Sood, *ACS Nano*, 2010, **4**, 1687-1695.
- 16 D. S. Sholl and K. A. Fichthorn, *J. Chem. Phys.*, 1997, **107**, 4384-4389.

- 17 C. D. Ball, N. D. MacWilliam, J. K. Percus and R. K. Bowles, *J. Chem. Phys.*, 2009, **130**, 054504.
- 18 K. K. Mon and J. K. Percus, *J. Chem. Phys.*, 2000, **112**, 3457-3458.
- 19 K. K. Mon and J. K. Percus, *J. Chem. Phys.*, 2002, **117**, 2289-2292.
- 20 K. K. Mon and J. K. Percus, *J. Chem. Phys.*, 2003, **119**, 3343-3346.
- 21 K. K. Mon and J. K. Percus, *J. Chem. Phys.*, 2005, **122**, 214503.
- 22 K. K. Mon and J. K. Percus, *J. Chem. Phys.*, 2006, **125**, 244704.
- 23 K. K. Mon and J. K. Percus, *J. Phys. Chem. C*, 2007, **111**, 15995-15997.
- 24 K. K. Mon and J. K. Percus, *J. Chem. Phys.*, 2007, **127**, 094702.
- 25 K. K. Mon, J. K. Percus and J. Yan, *Mol. Simul.*, 2003, **29**, 721-726.
- 26 J. K. Percus, *Phys. Rev. A*, 1974, **9**, 557-559.
- 27 K. Hahn and J. Kärger, *J. Phys. Chem.*, 1996, **100**, 316-326.
- 28 K. Hahn and J. Kärger, *J. Phys. Chem. B*, 1998, **102**, 5766-5771.
- 29 Y. C. Liu, J. D. Moore, T. J. Roussel and K. E. Gubbins, *Phys. Chem. Chem. Phys.*, 2010, **12**, 6632-6640.
- 30 Y.-C. Liu, J. D. Moore, Q. Chen, T. Roussel, Q. Wang and K. E. Gubbins, Crossover from Single-File to Fickian Diffusion in Carbon Nanotubes and Nanotube Bundles: Pure Components and Mixtures, in *Diffusion Fundamentals III*, ed. C. Chmelik, N. Kanelopoulos, J. Kärger and D. Theodorou, Leipziger Universitätsverlag, Athens, 2009, pp. 164-180.
- 31 A. Striolo, *Nano Lett.*, 2006, **6**, 633-639.
- 32 Z. G. Mao and S. B. Sinnott, *J. Phys. Chem. B*, 2000, **104**, 4618-4624.

- 33 F. J. A. L. Cruz and E. A. Muller, *Adsorption*, 2009, **15**, 13-22.
- 34 S. K. Bhatia, H. B. Chen and D. S. Sholl, *Mol. Simul.*, 2005, **31**, 643-649.
- 35 J. D. Moore, J. C. Palmer, Y. C. Liu, T. J. Roussel, J. K. Brennan and K. E. Gubbins, *Appl. Surf. Sci.*, 2010, **256**, 5131-5136.
- 36 B. Coasne, S. K. Jain and K. E. Gubbins, *Mol. Phys.*, 2006, **104**, 3491-3499.
- 37 T. X. Nguyen, S. K. Bhatia, S. K. Jain and K. E. Gubbins, *Mol. Simul.*, 2006, **32**, 567-577.
- 38 J. Pikunic and K. E. Gubbins, *Eur. Phys. J. E*, 2003, **12**, 35-40.
- 39 J. Karger, H. Pfeifer, R. S. Vartapetian and A. M. Voloshchuk, *Pure Appl. Chem.*, 1989, **61**, 1875-1880.
- 40 A. I. Skoulidas and D. S. Sholl, *J. Phys. Chem. B*, 2002, **106**, 5058-5067.
- 41 W. A. Steele, *The Interaction of Gases with Solid Surfaces*, Pergamon Press, Oxford, New York,, 1974.
- 42 N. Hamada, S. Sawada and A. Oshiyama, *Phys. Rev. Lett.*, 1992, **68**, 1579-1581.
- 43 J. C. Phillips, R. Braun, W. Wang, J. Gumbart, E. Tajkhorshid, E. Villa, C. Chipot, R. D. Skeel, L. Kale and K. Schulten, *J. Comput. Chem.*, 2005, **26**, 1781-1802.
- 44 K. E. Gubbins and J. D. Moore, *Ind. Eng. Chem. Res.*, 2010, **49**, 3026-3046.
- 45 Y. C. Liu, J. W. Shen, K. E. Gubbins, J. D. Moore, T. Wu and Q. Wang, *Phys. Rev. B*, 2008, **77**, 125438.
- 46 N. Chennamsetty, H. Bock and K. E. Gubbins, *Mol. Phys.*, 2005, **103**, 3185-3193.
- 47 M. Bazarnik, M. Cegiel, P. Biskupski, M. Jazdzewska, S. Mielcarek, M. Sliwinska-Bartkowiak and R. Czajka, *Central European Journal of Physics*, 2009, **7**, 295-298.

- 48 S. Jakobtorweihen, C. P. Lowe, F. J. Keil and B. Smit, *J. Chem. Phys.*, 2007, **127**, 024904.
- 49 D. Frenkel and B. Smit, *Understanding Molecular Simulation: From Algorithms to Applications*, Academic Press, San Diego, 2002.
- 50 G. S. Grest and K. Kremer, *Phys. Rev. A*, 1986, **33**, 3628-3631.
- 51 Y.-C. Liu, J. D. Moore, Q. Chen, T. J. Roussel, Q. Wang and K. E. Gubbins, in *Proceedings of Diffusion Fundamentals III*, ed. C. Chmelik, N. Kanellopoulos, J. Kärger and D. Theodorou, Leipziger Universitätsverlag, Athens, Greece, 2009, 164-182.
- 52 H. J. C. Berendsen, J. P. M. Postma, W. F. Vangunsteren, A. Dinola and J. R. Haak, *J. Chem. Phys.*, 1984, **81**, 3684-3690.
- 53 H. C. Andersen, *J. Chem. Phys.*, 1980, **72**, 2384-2393.
- 54 S. Jakobtorweihen, M. G. Verbeek, C. P. Lowe, F. J. Keil and B. Smit, *Phys. Rev. Lett.*, 2005, **95**, 044501.
- 55 S. Jakobtorweihen and F. J. Keil, *Mol. Simul.*, 2009, **35**, 90-99.
- 56 D. M. Ackerman, A. I. Skoulidas, D. S. Sholl and J. K. Johnson, *Mol. Simul.*, 2003, **29**, 677-684.
- 57 J. Li, T. Furuta, H. Goto, T. Ohashi, Y. Fujiwara and S. Yip, *J. Chem. Phys.*, 2003, **119**, 2376-2385.
- 58 M. Endo, K. Takeuchi, T. Hiraoka, T. Furuta, T. Kasai, X. Sun, C. H. Kiang and M. S. Dresselhaus, *J. Phys. Chem. Solids*, 1997, **58**, 1707-1712.
- 59 C. H. Kiang, M. Endo, P. M. Ajayan, G. Dresselhaus and M. S. Dresselhaus, *Phys. Rev. Lett.*, 1998, **81**, 1869-1872.

- 60 E. Lindahl, B. Hess and D. van der Spoel, *J. Mol. Model.*, 2001, **7**, 306-317.
- 61 S. Plimpton, *J. Comput. Phys.*, 1995, **117**, 1-19.
- 62 J. H. Walther, R. Jaffe, T. Halicioglu and P. Koumoutsakos, *J. Phys. Chem. B*, 2001, **105**, 9980-9987.
- 63 J. K. Johnson, J. A. Zollweg and K. E. Gubbins, *Mol. Phys.*, 1993, **78**, 591-618.
- 64 A. I. Skoulidas, D. M. Ackerman, J. K. Johnson and D. S. Sholl, *Phys. Rev. Lett.*, 2002, **89**, 185901.
- 65 G. Arya, H. C. Chang and E. J. Maginn, *Mol. Simul.*, 2003, **29**, 697-709.
- 66 T. Duren, F. J. Keil and N. A. Seaton, *Mol. Phys.*, 2002, **100**, 3741-3751.
- 67 V. P. Sokhan, D. Nicholson and N. Quirke, *J. Chem. Phys.*, 2002, **117**, 8531-8539.
- 68 V. P. Sokhan, D. Nicholson and N. Quirke, *J. Chem. Phys.*, 2004, **120**, 3855-3863.
- 69 A. Marmier, H. Spohr, D. J. Cooke, S. Kerisit, J. P. Brodholt, P. B. Wilson and S. C. Parker, *Mol. Simul.*, 2005, **31**, 385-389.
- 70 H. B. Chen, J. K. Johnson and D. S. Sholl, *J. Phys. Chem. B*, 2006, **110**, 1971-1975.
- 71 D. Dubbeldam and R. Q. Snurr, *Mol. Simul.*, 2007, **33**, 305-325.
- 72 J. J. Zhu, J. L. Figueiredo and J. L. Faria, *Catal. Commun.*, 2008, **9**, 2395-2397.
- 73 Y. P. Zhou, Y. X. Wang, H. H. Chen and L. Zhou, *Carbon*, 2005, **43**, 2007-2012.
- 74 B. Kastening and M. Heins, *Electrochim. Acta*, 2005, **50**, 2487-2498.
- 75 Y. El-Sayed and T. J. Bandosz, *J Colloid Interf Sci*, 2001, **242**, 44-51.
- 76 J. C. Palmer, J. K. Brennan, M. M. Hurley, A. Balboa and K. E. Gubbins, *Carbon*, 2009, **47**, 2904-2913.

- 77 G. Opletal, T. Petersen, B. O'Malley, I. Snook, D. G. McCulloch, N. A. Marks and I. Yarovsky, *Mol. Simul.*, 2002, **28**, 927-938.
- 78 S. K. Jain, R. J. M. Pellenq, J. P. Pikunic and K. E. Gubbins, *Langmuir*, 2006, **22**, 9942-9948.
- 79 R. Ryoo, S. H. Joo and S. Jun, *J. Phys. Chem. B*, 1999, **103**, 7743-7746.
- 80 R. Ryoo, S. H. Joo, M. Kruk and M. Jaroniec, *Adv. Mater.*, 2001, **13**, 677-681.
- 81 T. Kyotani, Z. X. Ma and A. Tomita, *Carbon*, 2003, **41**, 1451-1459.
- 82 T. Roussel, C. Bichara, K. E. Gubbins and R. J. M. Pellenq, *J. Chem. Phys.*, 2009, **130**, 174717.
- 83 T. Roussel, A. Didion, R. J. M. Pellenq, R. Gadiou, C. Bichara and C. Vix-Guterl, *J. Phys. Chem. C*, 2007, **111**, 15863-15876.
- 84 K. Hahn and J. Karger, *J. Phys. Chem.*, 1996, **100**, 316-326.
- 85 S. Jakobtorweihen, F. J. Keil and B. Smit, *J. Phys. Chem. B*, 2006, **110**, 16332-16336.
- 86 B. Coasne, S. K. Jain and K. E. Gubbins, *Eur. Phys. J. Special Topics*, 2007, **141**, 121-125.
- 87 J. Pikunic and K. E. Gubbins, *Eur. Phys. J. E*, 2003, **12**, 35-40.
- 88 S. Brandani, D. M. Ruthven and J. Karger, *Zeolites*, 1995, **15**, 494-495.
- 89 K. Hahn and J. Karger, *J. Phys. Chem. B*, 1998, **102**, 5766-5771.
- 90 L. D. Gelb and K. E. Gubbins, *Langmuir*, 1999, **15**, 305-308.
- 91 M. Schoen and C. Hoheisel, *Mol. Phys.*, 1984, **52**, 1029-1042.
- 92 M. Schoen and C. Hoheisel, *Mol. Phys.*, 1984, **52**, 33-56.
- 93 L. Onsager, *Phys. Rev.*, 1931, **38**, 2265-2279.

- 94 L. Onsager, *Phys. Rev.*, 1931, **37**, 405-426.
- 95 J. Stefan, *Sitzungsberichte der Kaiserlichen Akademie der Wissenschaften Wien, 2te Abteilung a.*, 1871, **63**, 63-124.
- 96 J. C. Maxwell, *Philos. Mag.*, 1868, **35**, 129-145.
- 97 R. Krishna and J. M. van Baten, *Chem. Eng. Sci.*, 2008, **63**, 3120-3140.
- 98 D. N. Theodorou, R. Q. Snurr and A. T. Bell, in *Comprehensive Supramolecular Chemistry*, ed. G. Alberti and T. Bein, Pergamon, Oxford, 1996, vol. 7, pp. 507-548.